SANDIA REPORT

SAND2012-7985
Unlimited Release
September, 2012

Modeling, sensor design, and performance predictions for gas filter correlation radiometers

Jeffrey A. Mercier, Mark W. Smith, Jeffery P. Hunt, Aaron M. Ison

Sandia National Laboratories

Modeling, sensor design, and performance predictions for gas filter correlation radiometers

Jeffrey A. Mercier, Mark W. Smith, Dept. 5717
Jeffery P. Hunt, Dept. 5712, Aaron M. Ison, Dept. 2617
Sandia National Laboratories
P.O. Box 5800
Albuquerque, New Mexico 87185-MS0406

Abstract

Gas filter correlation (GFC) radiometry is a technique for detecting and measuring a specific gas or a small suite of gases. The GFC approach combines extremely high spectral resolution with high optical throughput (or etendue) while avoiding the stringent alignment and mechanical stability requirements imposed by interferometric measurements. The GFC approach is well matched to staring imagers and is very efficient in terms of data volume and bandwidth. A primary limitation to GFC for atmospheric remote sensing is the fact that it works best with gases that have strong absorption features but that are present in small concentrations. This report describes a software model that was developed to predict the performance of GFC sensors. This report presents a design for an airborne GFC sensor and predicts the ability of this sensor and a hypothetical satellite sensor to measure methane in the atmosphere.

ACKNOWLEDGMENTS

CONTENTS

FIGURES

TABLES

6

NOMENCLATURE

1-D	one dimensional
2-D	two dimensional
COTS	commercial, off-the-shelf
CFD	computational fluid dynamics
CTE	coefficient of thermal expansion
FOV	field-of-view
FPA	focal plane array
GFC	gas filter correlation
GIFOV	ground instantaneous field-of-view
IFOV	instantaneous field-of-view
LBL	line by line
MODTRAN	MODerate resolution TRANsmittance (Atmospheric transmission code)
NASA	National Aeronautics and Space Administration
OCO	Orbiting Carbon Observatory
PEG	photo-electron generation
RT	radiative transport
SAMM2	SHARC and MODTRAN Merged Code version 2 (transmission code)
SWIR	short wave infrared
UAV	unmanned aerial vehicle

1. INTRODUCTION

The sections of this introduction provide a general overview of gas filter correlation radiometry, explain how this technique can be applied to remotely sensed atmospheric trace gases, and describe the radiometric nomenclature and conventions used in this document.

1.1. Gas filter correlation (GFC) radiometry

Gas filter correlation radiometry is a simple way to implement a filter that has very high spectral resolution that is matched to the absorption features of a specific gas of interest. Figure 1 shows a schematic diagram of a basic gas filter correlation radiometer that uses two optical channels that are focused on the same scene. The two channels use band pass filters, which are as identical as possible, to isolate the same general spectral region of interest, which includes one or more absorption lines of the gas of interest. Each channel also includes a gas cell. The cell in one channel is filled with a sample of the gas of interest while the cell in the other channel is filled with an optically inactive reference gas. Light that passes through the two different cells is sent to two different detectors. The detectors can be 2-D arrays to produce images. The signal that is measured by the gas cell channel is subtracted from the signal measured by the reference channel cell. This creates a spectral response function that is equal to the difference in transmission for the two gas cells. For array detectors the subtraction is carried out pairwise with corresponding pixels.

Figure 1: Schematic diagram of a gas filter correlation radiometer.
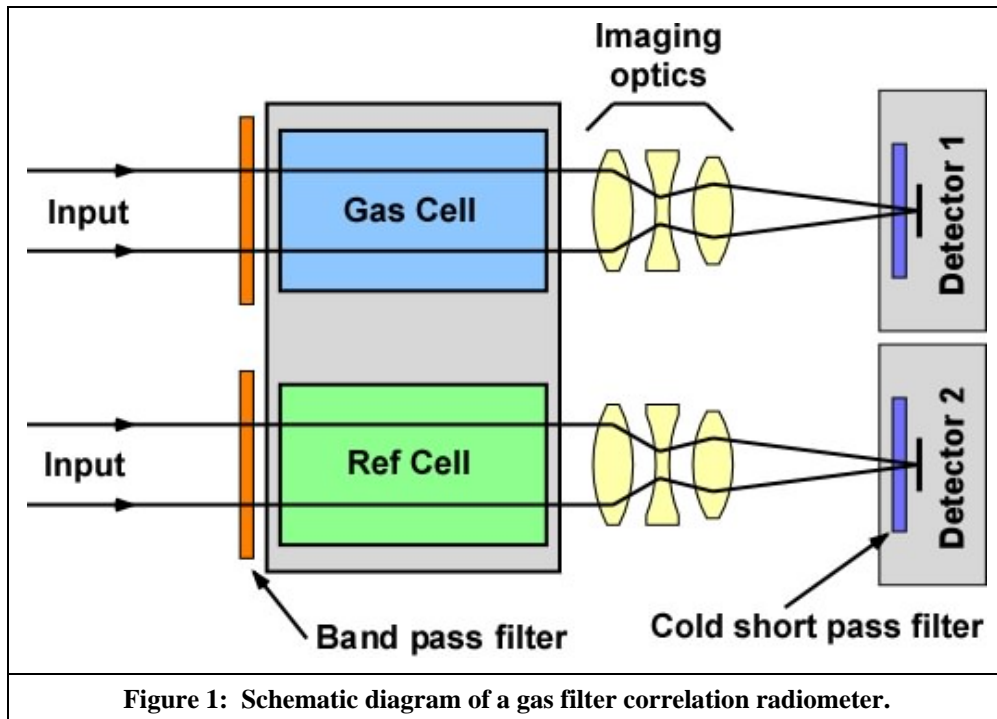
In general a cold short pass filter will be placed in front of each detector to cut down on thermal background radiation. There are thus actually three levels of spectral discrimination. First, the cold filter sets an upper limit to the detector response. Second, the band pass filters isolate a general spectral region of interest. Third, the gas cell and reference cell together produce a very high spectral resolution filtering effect that is matched to the absorption features of the gas of interest. Figure 2 illustrates how the matched, high resolution filter effect is produced. The

green line shows transmission for an optically inactive reference gas. The blue line shows transmission for one individual gas absorption line. The red line shows the difference in transmission between the two cells, which is the effective spectral response function for the cells. The spectral resolution of this difference function is approximately equal to the width of the absorption line in the reference cell. The resolving power, or ratio of center wavelength to spectral resolution, can easily reach a value of several hundred thousand.

Figure 2: Operation of gas filter correlation cells in the spectral domain.
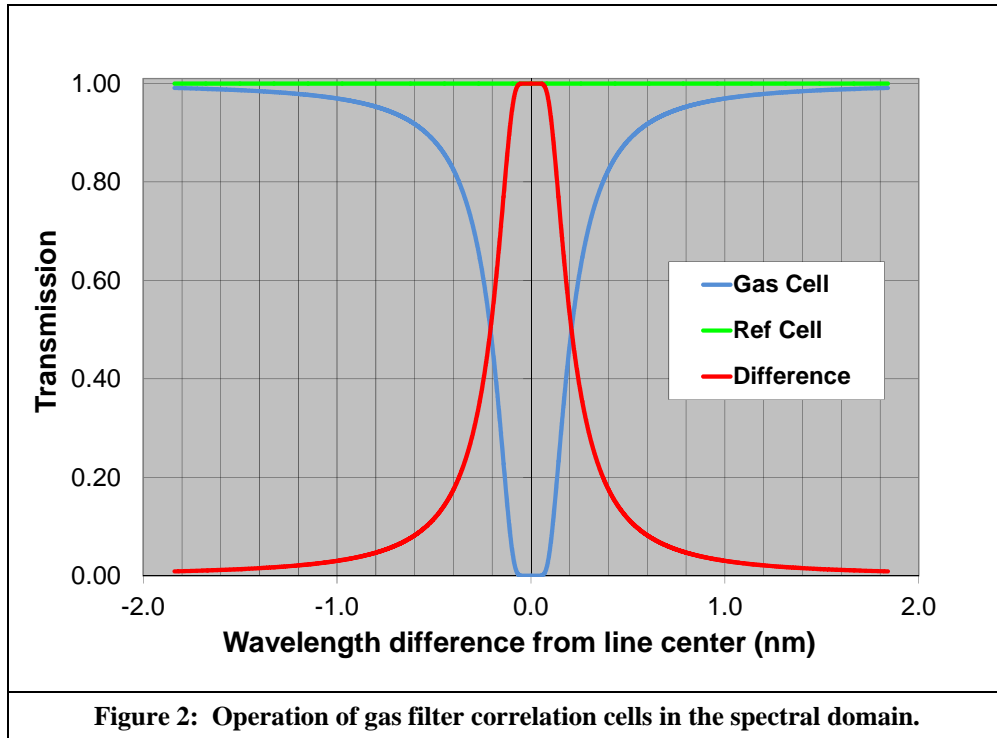
Gas correlation measurements have several attractive features. As just described the effective spectral resolution is on the order of the line width of the gas in the absorption cell, which can be extremely narrow if the pressure in the absorption cell is low. This high resolution is achieved without the need to maintain the stringent dimensional precision of an interferometer. Furthermore, the spectral response of the gas correlation cell stays perfectly tuned to the spectral features of the gas of interest. Optical throughput can be quite large, as both the area of the cell and the acceptance angle can be large. Because the gas cell is simply an optical filter, it is straightforward to match the technique to a staring imager with a 2-D detector array or to a scanning imager with a 1-D array. Because only two signals (one for each of the gas cells) are produced per pixel, data volumes are much smaller than for typical hyperspectral approaches such as a Fourier transform interferometer.

1.2. Remote sensing with a GFC radiometer

Passive remote sensing of trace gases in the troposphere generally relies upon one of two physical processes. These processes are shown schematically in Figure 3. In one process, radiation is emitted by the sun, propagates down through the earth's atmosphere, and is then reflected or scattered at the earth's surface. Some of the radiation that has been scattered at the earth's surface is detected by a downward-looking remote sensing instrument. Radiation is absorbed along both the downward and upward paths by trace gases in the atmosphere, at

wavelengths that are characteristic of particular molecular species. In the other process, thermal radiation is emitted at the earth's surface, and is then partially absorbed and subsequently reemitted as it propagates upwards through the atmosphere, again at wavelengths characteristic of particular molecular species.
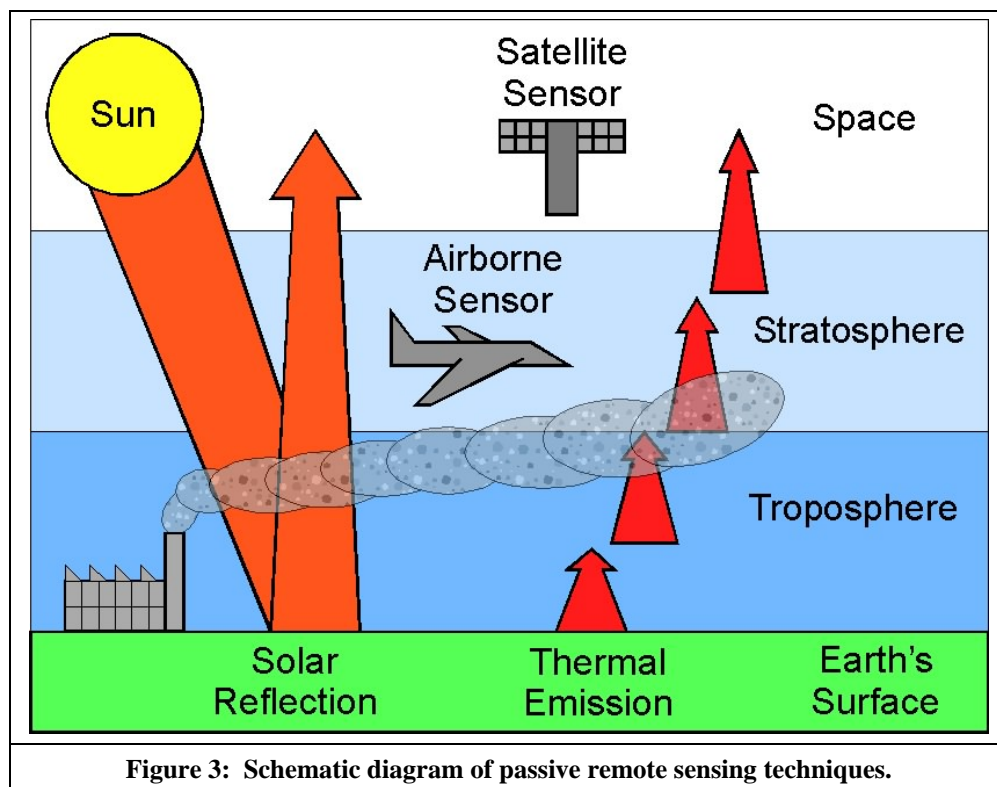
Figure 3: Schematic diagram of passive remote sensing techniques.

Gas filter correlation radiometry is a simple way to make measurements of the amount of radiation that is absorbed or emitted at specific wavelengths that are keyed precisely to the spectral features of specific gases of interest. Work completed under this LDRD has concentrated on using the absorption of solar reflected radiation to measure methane (CH_4) in the atmosphere. CH_4 is an important greenhouse gas and leaks from natural gas pipelines represent a significant loss of energy resources and revenue.

1.3. Remote nomenclature and conventions

The software models described in the next section of this document calculate the optical radiation field produced by a given scene and then calculate how much flux from this field flows through an optical sensor onto a detector. These calculations fall into the field of radiometry. Different scientific and engineering disciplines attach different meaning to radiometric terms such as "intensity", "flux", etc. An introduction to radiometric nomenclature and to the conventions followed in this document is therefore in order.

The quantities that are most significant in the radiometric models are radiance, irradiance, and flux. These quantities may be expressed using either Watts (W) or photons per second (ph s^{-1}). The models described in this document use a quantum efficiency factor, rather than a power response factor, to describe detector response to optical radiation. The models also use detector integration times and frame summing rather than frequency response and filtering in the

frequency domain. Therefore all radiometric calculations are performed in units of photons per second rather than Watts.

Most radiometric quantities may be expressed as spectral values or as band integrated values. The instrument always responds physically to band integrated quantities. However, the models use spectrally resolved quantities at intermediate stages of the calculations. The symbols used to denote spectrally resolved quantities are:

$L(\lambda) = $ spectrally resolved radiance in units of ph s^{-1} cm^{-2} sr^{-1} μm^{-1}

$E(\lambda) = $ spectrally resolved irradiance in units of ph s^{-1} cm^{-2} μm^{-1}

$\Phi(\lambda) = $ spectrally resolved flux in units of ph s^{-1} μm^{-1}

The symbols used to denote band integrated quantities are:

$L^{bnd} = $ band integrated radiance in units of ph s^{-1} cm^{-2} sr^{-1}

$E^{bnd} = $ band integrated irradiance in units of ph s^{-1} cm^{-2}

$\Phi^{bnd} = $ band integrated flux in units of ph s^{-1} μm^{-1}

Dimensional analysis is a handy tool in radiometry, and it can be useful to associate specific units with different elements of the model. The final result of all of the scene calculations is the spectral radiance (ph s^{-1} cm^{-2} sr^{-1} μm^{-1}) presented by the scene to the entrance pupil of the sensor. The sensor modules multiply this spectrally resolved radiance by various spectral transmission factors (dimensionless) and then integrate as a function of wavelength to produce a band integrated radiance (ph s^{-1} cm^{-2} sr^{-1}). This quantity is then multiplied by the collection area (cm^2) of the entrance pupil and by a solid angle (sr) factor per pixel to produce a band integrated flux per pixel (ph s^{-1} pix^{-1}). The photon flux per pixel is then multiplied by a quantum efficiency factor (electrons per photon) to yield a photo-electron generation (PEG) rate with units of photo-electrons per second per pixel (pe s^{-1} pix^{-1}). The band integrated PEG rate is then multiplied by an integration time to find the number of electrons generated per detector pixel for a single readout of the detector. The model tracks the number of electrons generated from solar radiance versus thermally generated background radiance versus detector dark current, although of course the detector and its read out electronics do not know the difference.

2. RADIOMETRIC MODELS

Figure 4 shows the overall architecture of the radiometric models used predict performance for various gas filter correlation (GFC) sensors that observe some gas of interest in the atmosphere. Elements that are color coded blue in Figure 4 represent inputs to the models, elements that are color coded green represent calculations performed by the models, and the yellow element represents the output file.
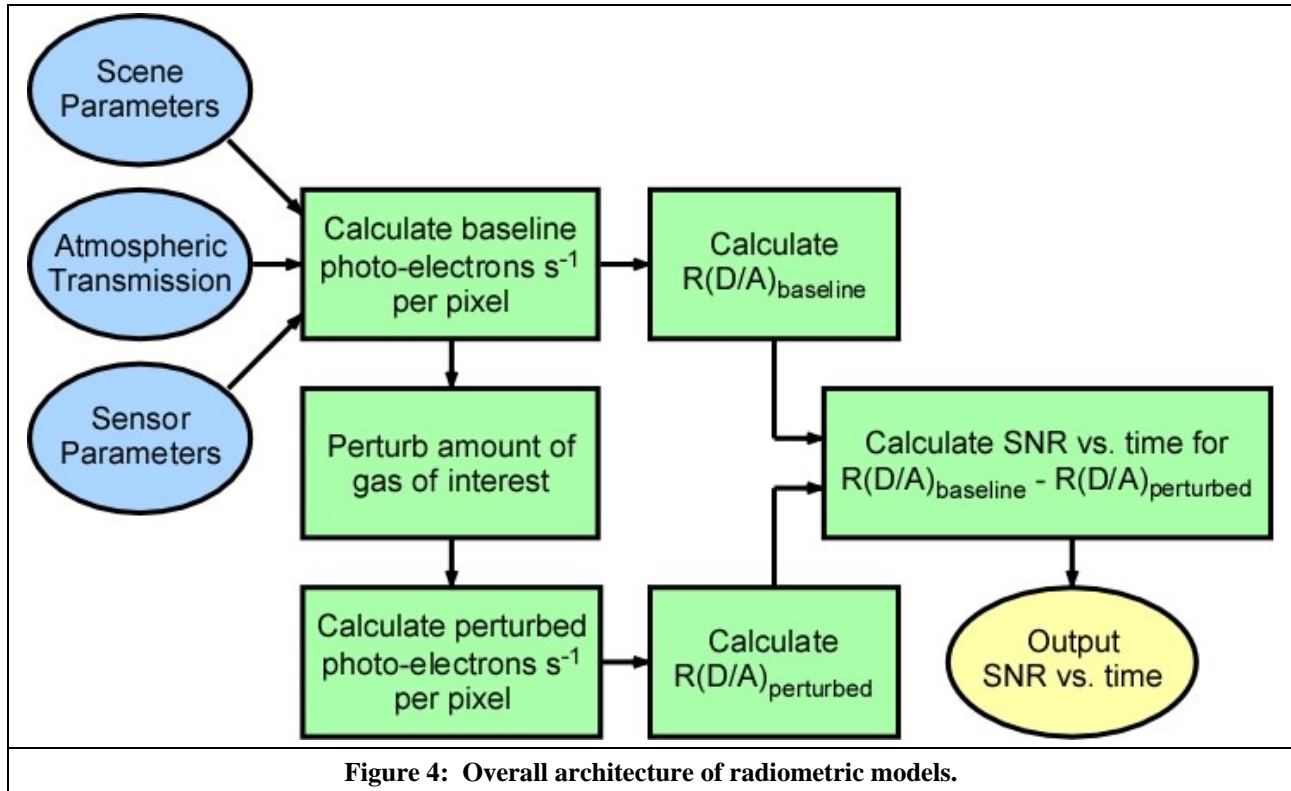
Figure 4: Overall architecture of radiometric models.

A pair of radiometric models of the GFC remote sensing process were developed under this LDRD. The primary difference between the two models lies in how the amount of the gas of interest in the scene is perturbed. One model assumes that the gas of interest is distributed throughout the atmospheric column according to some prescribed profile of concentration as a function of altitude. It then perturbs the concentration profile at all altitudes by increasing it by a specified ratio. This is a good approach for predicting the performance of a sensor that would make global measurements of the column amount of CH_4 in order to study greenhouse gases. The other model perturbs the concentration profile by adding a plume with a specified product of concentration $\times$ path length. This is a good approach for predicting the performance of a sensor that would inspect natural gas pipelines for leaks. In the remainder of this document these are called the column model and the plume model for short.

2.1. Scene components

The equation that describes the spectrally resolved solar radiance from the scene for the baseline concentration profile is:

$$L_{bS}(\lambda) = \left[\frac{E_{xS}(\lambda) \times \cos(\theta_S) \times A(\lambda)}{\pi}\right] \times \left[\prod_{n=1}^{N} \tau_n(\lambda;\theta_S)\right] \times \left[\prod_{n=1}^{N} \tau_n(\lambda;\theta_V)\right] \qquad (2.1)$$

where λ is wavelength, $L_{bS}(\lambda)$ is the baseline spectrally resolved solar radiance as a function of wavelength, $E_{xS}(\lambda)$ is spectrally resolved exo-atmospheric solar irradiance, θ_S is the solar zenith angle, θ_V is the sensor view angle, $A(\lambda)$ is the scene albedo, $\tau_n(\lambda;\theta_S)$ is the transmission factor for the n-th gas in the atmosphere calculated for a slant path angle of θ_S, and $\tau_n(\lambda;\theta_V)$ is the transmission factor for the n-th gas in the atmosphere calculated for a slant path angle of θ_V. The total number of gas transmission factors is equal to N. The models generally require three separate gas transmission factors– the first is for the gas of interest, the second is for water vapor, and the third is for a general collection of background gases.

In the column model the equation that describes the spectrally resolved solar radiance from the scene for the perturbed concentration profile is the same as the equation that describes the baseline radiance except that the transmission for the gas of interest, with a subscript of $n = 1$, is raised to the power r, which is the perturbation ratio applied to the column profile of the gas of interest. A perturbation ratio of, for example, r = 1.01 specifies that the model is to adjust transmission as if the profile of the gas of interest increased uniformly by the ratio of 1.01 (i.e., by 1%) at all altitudes in the atmosphere. This adjustment can be expressed by the substitutions:

$$\tau_1(\lambda;\theta_S) \rightarrow \tau_1^r(\lambda;\theta_S) \qquad (2.2a)$$

$$\tau_1(\lambda;\theta_V) \rightarrow \tau_1^r(\lambda;\theta_V) \qquad (2.2b)$$

In the plume model the equation that describes the spectrally resolved solar radiance from the scene perturbed by the addition of a plume of gas is:

$$L_{pS}(\lambda) = L_{bS}(\lambda) \times \tau_p(\lambda;\theta_S) \times \tau_p(\lambda;\theta_V) \qquad (2.3)$$

where $L_{pS}(\lambda)$ is the perturbed radiance as a function of wavelength, λ, $L_{bS}(\lambda)$ is the baseline spectrally resolved solar radiance, $\tau_p(\lambda;\theta_S)$ is the transmission factor for the gas plume calculated for solar zenith angle θ_S, and $\tau_p(\lambda;\theta_V)$ is the transmission factor for the gas plume calculated for sensor view angle θ_V.

2.1.1. Emission of solar radiation by the sun

The sun is modeled as a 5800 K black body and a version of the Planck function for blackbody radiation is used to calculate spectrally resolved solar radiance in units of ph s^{-1} cm^{-2} sr^{-1}. Solar radiance is converted to exo-atmospheric solar irradiance by multiplying by a solid angle factor of 6.773e^{-5} steradians, which corresponds to the full angle of just over 0.532^o that the sun subtends when viewed from the mean distance between the sun and the earth.

2.1.2. Attenuation of solar radiation in the atmosphere

Various mechanisms attenuate solar radiation in the earth's atmosphere. Absorption by gases in the atmosphere is the mechanism that is most directly relevant to optical remote sensing by means of gas filter correlation radiometry. This includes not only absorption by the gas of interest but also absorption by interfering species such as water vapor. Line-by-line calculations are required to produce results at sufficiently high spectral resolution to be useful for modeling

the gas correlation technique. The SAMM2 code is used for these calculations, which are the source of the various τ_n and τ_p of Eqs. (2.1) through (2.3). Interference by other industrial effluents (such as solvents or hydrocarbons) has not been included to date, but could be added.

Scattering, by aerosols and by clouds, is another significant mechanism by which solar radiation is attenuated as it passes through the earth's atmosphere. As a general rule scattering by aerosols is relatively insignificant compared to molecular absorption at short wave infrared (SWIR) wavelengths and so the GFC models ignore this effect. The models also assume cloud free conditions along its single line-of-sight.

2.1.3. Reflection of solar radiation at the earth's surface

Reflection of solar radiation at the surface of the earth can more generally be called a scattering process, especially for the common situation of diffuse reflection by a rough surface. Surface albedo, $A(\lambda)$, varies slowly as a function of wavelength compared to molecular absorption and so only moderate spectral resolution is required for this portion of the model. The GFC models use tabulated data extracted from MODTRAN to model surface albedo as a function of wavelength. The models at present performs calculations for only a single pixel, or single line-of-sight, but could be modified to take into account spatial variations of surface properties (i.e., scene clutter as described in section 4.1.4).

2.1.4. Emission of thermal radiation at the earth's surface

The signal for optical remote sensing at wavelengths < 3.0 μm comes primarily from solar radiation that is reflected at the surface of the earth as opposed to thermal radiation that is emitted by the surface of the earth. However, the models include thermal emission as a background term. The equation that is used to calculate spectrally resolved thermal radiance is:

$$L_T(\lambda) = \varepsilon(\lambda) \times L_{BB}(\lambda; T) \tag{2.4}$$

where $L_T(\lambda)$ is spectrally resolved thermal radiance as a function of wavelength, λ, $\varepsilon(\lambda)$ is the emissivity, and $L_{BB}(\lambda; T)$ is the spectrally resolved radiance for a blackbody at temperature T calculated as a function of wavelength by the Plank radiation function. Emissivity is derived from albedo as $\varepsilon(\lambda) = 1 - A(\lambda)$. The surface albedo, $A(\lambda)$, was described in the previous sub-section.

2.1.5. Attenuation and re-emission of thermal radiation in the atmosphere

The models do not at present take into account modification by the atmosphere of the thermal radiation that is emitted by surfaces in the scene. This is equivalent to assuming that the atmosphere is at the same temperature as the ground. This is a reasonable assumption for a sensor that is close to the ground, but is overly simplistic for a sensor that is high overhead in an aircraft or on a satellite platform. Because the atmosphere gradually cools as a function of altitude the net thermal radiation that reaches an airborne or space based sensor will in reality be somewhat less than what leaves the ground.

2.2. Sensor components of model

This section of the document describes how the GFC sensor is modeled. The column and plume models treat the sensor in identical fashion. The basic operations carried out by the sensor

components of the models are as follows. The spectrally resolved scene radiance, which was calculated according to Eq. (2.1) through (2.3) is multiplied by various spectral transmission factors and then integrated as a function of wavelength to produce a band integrated radiance:

$$L^{bnd} = \int_{\lambda_{\min}}^{\lambda_{\max}} L(\lambda) \times \left[\prod_{m=1}^{M} t_m(\lambda) \right] d\lambda \qquad (2.5)$$

where L^{bnd} is a band integrated radiance, $L(\lambda)$ is a spectrally resolved radiance, $t_m(\lambda)$ is the transmission of the m-th optical element as a function of wavelength, and M is the total number of optical elements through which radiation passes inside the sensor. Note that one of the $t_m(\lambda)$ represents either the gas correlation cell or the reference cell. At present a number of analytical formulas are used to calculate transmission as a function of wavelength to produce $t_m(\lambda)$ values for various filters and other optical elements. This is a convenient way to handle hypothetical sensors and to investigate sensor design options. However, for an actual sensor the analytical formulas should be replaced by measured values as these become available.

The band integrated radiance is multiplied by the collection area (cm^2) of the entrance pupil and by a solid angle (sr) factor per pixel to produce a band integrated flux per pixel:

$$\Phi^{bnd} = A \times \Omega \times L^{bnd} \qquad (2.6)$$

where Φ^{bnd} is the band integrated photon flux per pixel (with units of photons per second per pixel), A is the collection area of the entrance pupil, Ω is the solid angle of the cone of illumination for a single pixel, and L^{bnd} is a band integrated radiance. The $A\Omega$ product is oftentimes called the system throughput or etendue. The photon flux is next converted to a photo-electron generation rate:

$$\text{PEG} = \eta \times \Phi^{bnd} \qquad (2.7)$$

where PEG denotes photo-electron generation rate, η is the quantum efficiency of the detector, and Φ^{bnd} is the band integrated photon flux per pixel from Eq. (2.6). The PEG rates have units of photo-electrons per second per pixel (pe s^{-1} pix^{-1}) and must be multiplied by a data collection time to yield total number of electrons generated during a given observation time.

The following sections describe in slightly greater detail how the models treat various elements of a gas filter correlation sensor.

2.2.1. Array detectors

At present the models use only a single quantum efficiency factor that is independent of wavelength as a multiplicative factor in Eq. (2.7). This is obviously an approximation. If values of quantum efficiency were available as a function of wavelength then η (λ) could be moved into the integral of Eq. (2.5).

Likewise the values used at present for full well capacity, dark current, and read noise are estimates based on typical values provided by various detector manufacturers.

The full well capacity of individual detector pixels sets an upper limit to the allowable integration time which may be different than value set by the read out electronics:

$$\max\left[T^{\text{int}}\right] = \min\left\{T^{\text{int}}_{electronic}; \frac{W_c}{\left(\text{PEG}_S + \text{PEG}_T + i_d\right)}\right\} \qquad (2.8)$$

where $\max[\text{T}^{\text{int}}]$ is the maximum possible integration time to avoid saturation, $T^{\text{int}}_{electronic}$ is the maximum integration time as set by the detector electronics, W_c is the full well capacity, PEG_S is the photo-electron generation rate due to solar radiance, PEG_T is the photo-electron generation rate due to thermal radiance, and i_d is the detector dark current.

2.2.2. Short pass cold filter

The short pass cold filter is modeled analytically using a hyperbolic tangent function. The wavelengths at which transmission equals 95% and 5% are specified and then parameters in the hypberbolic tangent function are set to produce these characteristics. Out-of-band leakage is also specified for the blocking region. The analytical formula is convenient for performing trade studies but once the filter has been procured and characterized for a specific sensor the analytical formula should be replaced by measured data.

2.2.3. Band pass filters

The band pass filters are modeled analytically as a 4th order Butterworth filter, symmetrical about a specified center wavelength and with a specified full width at half maximum (FWHM). The center wavelength and FWHM have been varied systematically to optimize the filter pass bands. Again, once filters are procured and characterized for a specific sensor the analytical formula should be replaced by measured data.

2.2.4. Gas correlation cell

The same SAMM2 line-by-line code that is used to calculate molecular absorption in the atmosphere is used to calculate the transmission through the gas correlation cell. The reference cell is essentially optically transparent – its primary purpose is to maintain the optical balance between the two detector channels. However, the reference cell can be filled with another optically active gas so long as the absorption features of that gas do not overlap with the absorption features of the gas of interest.

2.2.5. Imaging optics

For the purpose of single pixel radiometric calculations we only need to use a few key parameters to calculate the system throughput, which is sometimes also called the area-solid angle (or $A\Omega$) product. The area can be the clear area of the entrance pupil, in which case the solid angle is derived from the field-of-view for a single pixel. Alternatively the area can be the area of a single pixel, in which case the solid angle is derived from the F/# of optics.

2.2.6. Self emission

Thermal self emission of radiation by the optics and the interior of the sensor is calculated using the standard Plank radiation function for a black body. The emissivity of the interior of the sensor is set to 1.0 and the emissivity of the optics is set to 1.0 minus their transmission.

3. SENSOR DESIGN

Preliminary design work was carried out for an airborne sensor. A basic optical layout was created using the Zemax ray trace program. A basic mechanical layout for mounting the sensor in an airborne pod was created. The following sections present a top level discussion of the optical and mechanical designs.

3.1. Optical design

The optical design uses three distinct optical channels that operate in parallel. One channel contains a gas cell filled with CH_4. A second channel contains a gas cell with an optically inactive reference gas. These two channels are shown schematically in Figure 1 and their function is described in Section 1.1. A third channel was added to measure water vapor, which has absorption lines interspersed throughout the CH_4 band, to allow for the correction of systematic errors due to interference from water vapor. Each channel contains an interference filter, a gas cell, an imaging lens, and an InSb array detector. The gas channel and reference channel use interference filters with pass bands that are as identical as possible. The water vapor channel uses a different pass band. Table 1 lists the first-order optical properties.

Table 1: Basic optical design parameters for airborne sensor.		
Parameter	**Value**	**Units**
Effective focal length	15	cm
Diameter of entrance pupil	7.5	cm
Wavelength range	2.25 to 2.50	µm
Full field of view	3.6×2.9	degrees
Size of detector array	320×256	pixels
Pixel pitch	30	µm
Ground instantaneous field-of-view	0.11	degrees

3.1.1. Lenses

A layout diagram of the lenses is shown in Figure 5. The lens materials are silicon and germanium. With AR coatings, the transmission for all three lenses will be greater than 80%. The optical aberrations are corrected well enough that the system has pixel-limited imaging performance. An ensquared energy plot for 30 micron pixels is shown in Figure 6.

Figure 5: Optical system layout.

Figure 6: Ensquared energy plot.
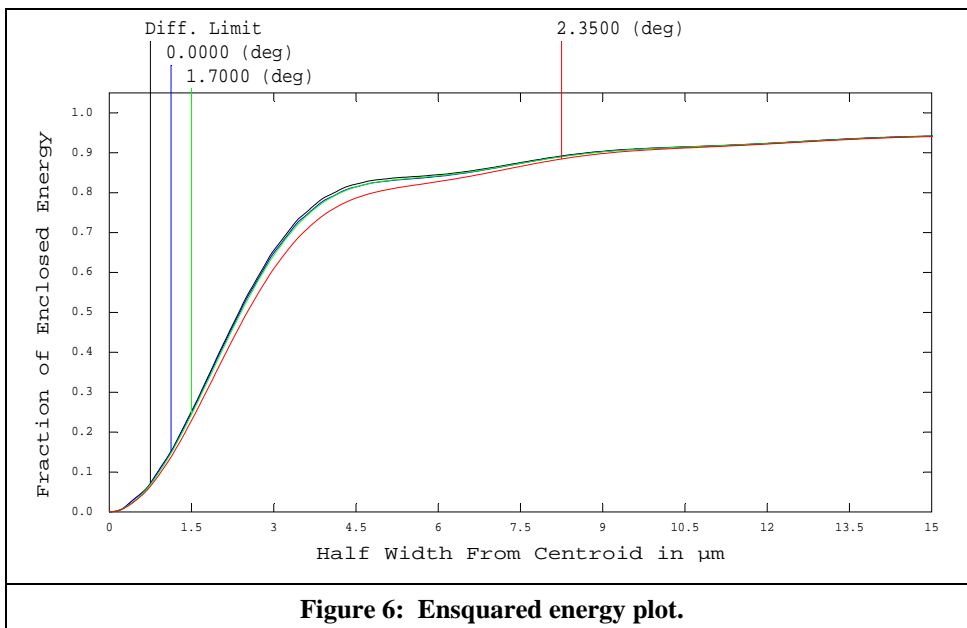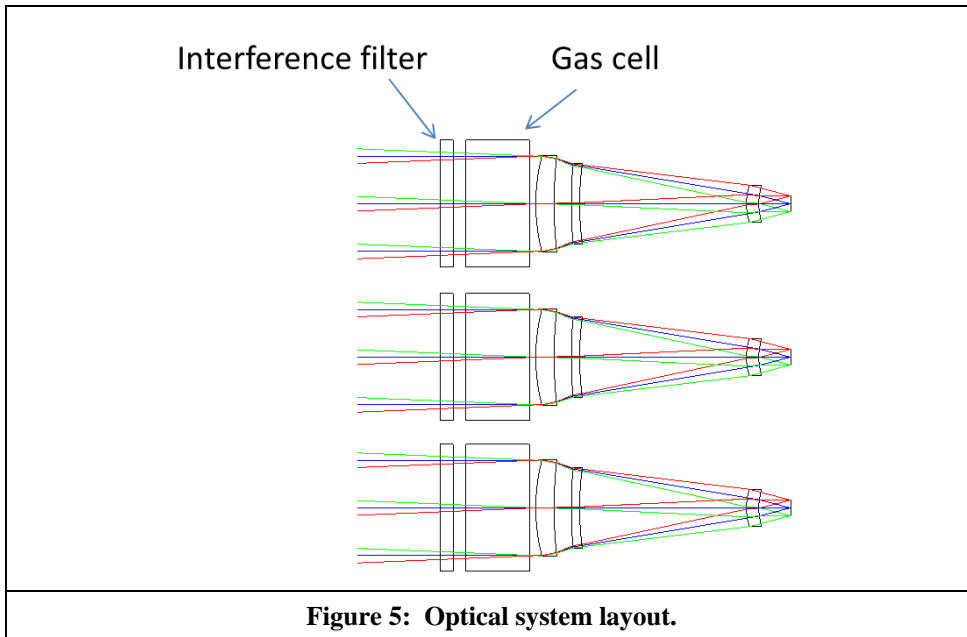
3.1.2. Filters

The spectral specifications for the narrow band filters are listed below. All filters use a silicon substrate and are designed to operate with +/- 4 degrees angle of incidence.

Table 2: Filter parameters for airborne sensor.		
	CH$_4$ and Ref Channels	Water Vapor Channel
Center wavelength (µm)	2.275	2.440
Half bandwidth (µm)	0.85	33
Peak transmission	≥ 90%	≥ 90%
Blocking	0.1%	0.1%

3.1.3. Detectors

The optics were designed to be used with a 320 x 256, 30 micron pitch InSb FPA. There are multiple COTS FPAs in this format. We have tentatively selected Indigo Systems model ISC9809.

3.2. Mechanical design

This mechanical design concept is based around an imaging system that will reside within a payload, which will be mounted to an aircraft pylon. A common form of these payloads is called a pod. A pod is an aerodynamic container that attaches to an aircraft's mounting pylons. The suggested vehicle for this system is the MQ-9 Reaper UAV. The vehicle payload capacity is used to define the acceptable pod size and weight for this system.

3.2.1. Aircraft Pod Interface

Reapers have three mounting pylons per wing (inboard, middle, and outboard), and are commonly referenced as station 1-6. The most spatially stable pylons are the inboard and middle (station 2-5), therefore these are the preferred mounting locations (optimally station 3 & 4). The inboard pylons have a payload capacity of 1500 lbs, the middle 600 lbs, and outboard 200 lbs. While the inboard pylons have the largest payload capacity, they also have the closest proximity to the landing struts. This close proximity drives maximum pod size, due to the landing strut flexing during takeoff and landing. The prescribed maximum pod diameter at this location is approximately 22 inches, and while a larger pod diameter is acceptable on the middle pylons, their acceptable payload weight is much less.
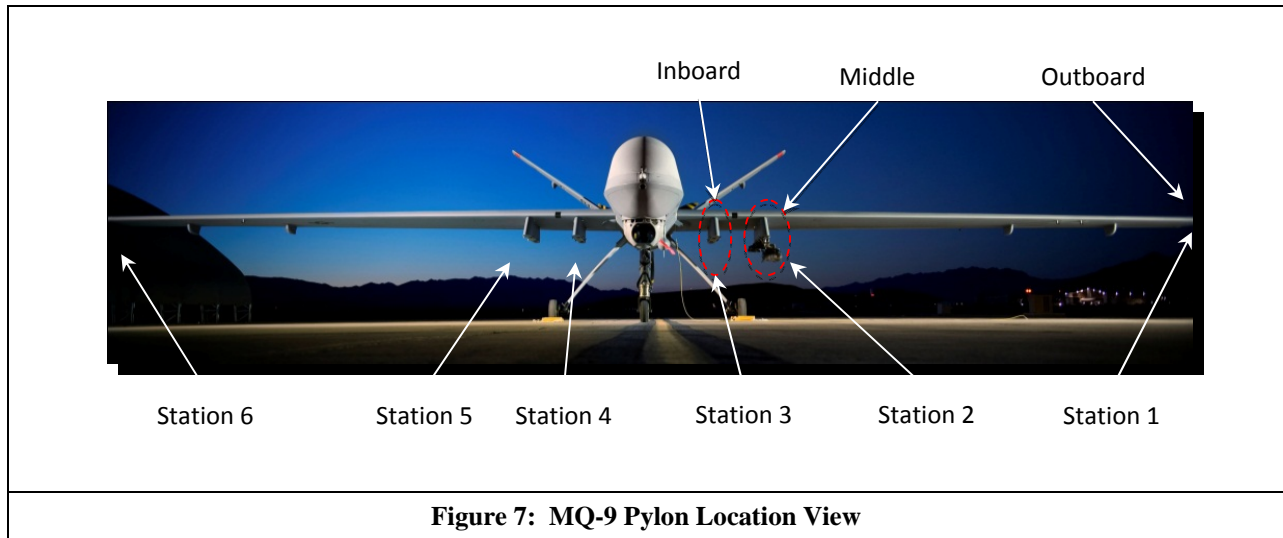
Figure 7: MQ-9 Pylon Location View

The pod concept is based on a standard pod design which contains a backbone, structural bulkheads, and a skin. The bulkheads are mounted to the backbone and each other, which provide structure for the pod skin. All components were designed to be aluminum to keep the overall system weight down. The pod and the skin would be a typical fiberglass or carbon composite, which is commonly used for these pods.
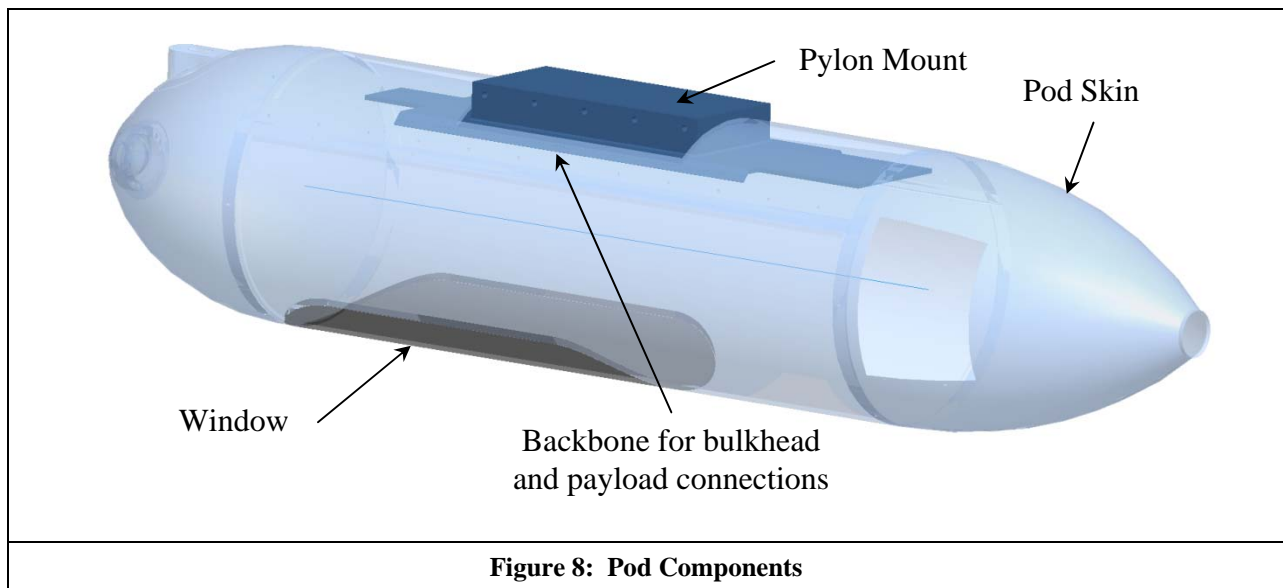
Figure 8: Pod Components

3.2.2. Opto-mechanical Pod Interface

For ease of alignment and assembly, the optomechanical structure concept was designed such that it is aligned and built separately from the pod structure. Once aligned, the optical payloads can then be assembled into the pod structure. Within the pod, there are two primary payloads: the forward optical payload and rear gimbal. The forward optical payload attaches to the pod backbone via an interface mount. The rear gimbal is mounted within a bulkhead for the pod structure itself. To allow light into the system, the base of the pod contains a window. The window will be mounted to the appropriate bulkheads and pod skin for structural containment.

Note: Pod structure bulk heads note shown for optical payload clarity

Window

Rear Gimbal

Forward Optical
Payload
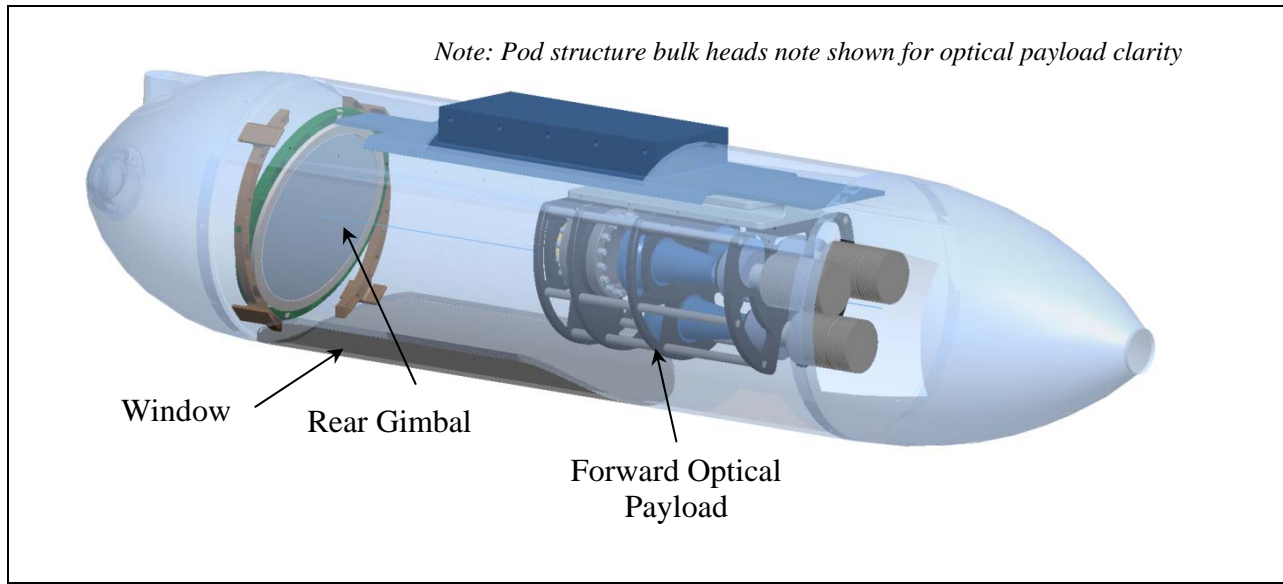
Figure 9: Airborne Pod Layout

The spacing between the rear gimbal and forward optical payload is 24 inches. This spacing allows for a forward pointing angle of up to 60°. A larger angle can be accommodated by elongating the pod structure and window length. This separation, combined with the forward optical payload length, drives the overall length of the pod to 7.2 feet. An acceptable maximum pod length can be on the order of 14 feet, therefore this length allows for expansion if necessary.

7.2ft

24 in

Moving
Direction

60°
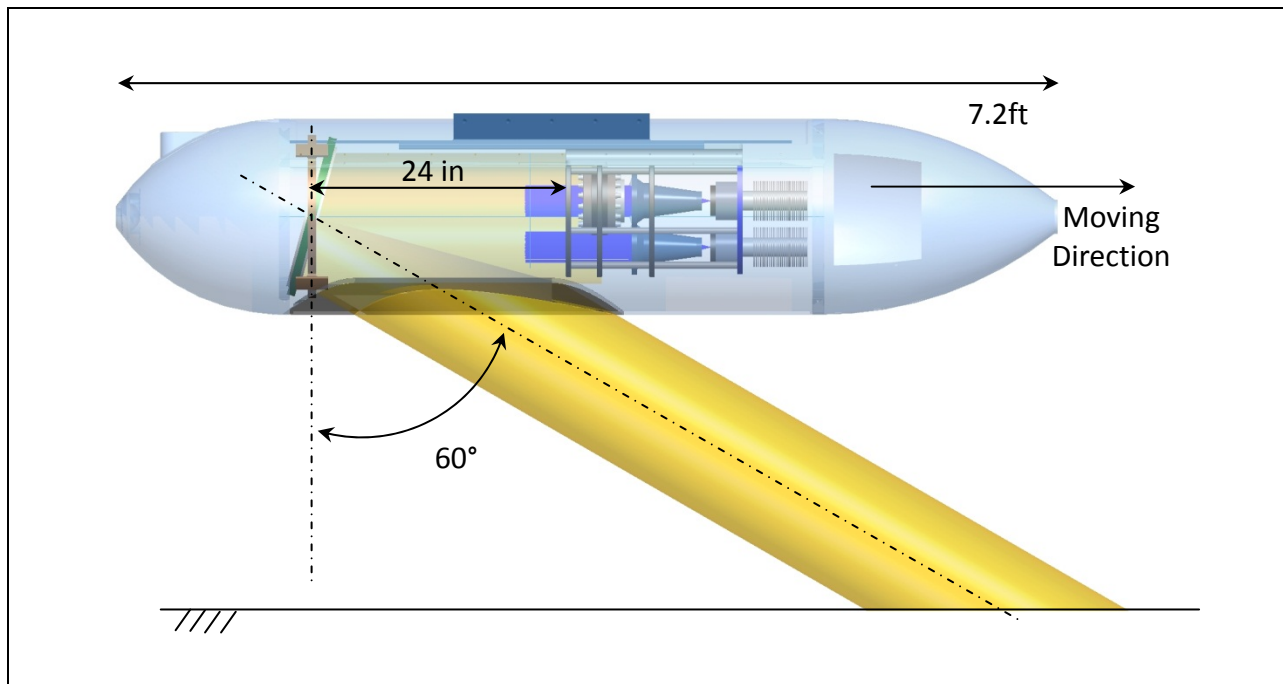
Figure 10: Forward Viewing Angle

3.2.2.1 Forward Optical Payload Structure

The forward optical payload structure consists of four distinct sections: filters, gas cells, focusing elements, and FPA bulkhead assemblies. Each respective section can be assembled prior to full

system integration. This structure lends itself to individual component assembly, which then comes together as a larger master assembly for final alignment. To accommodate the bulkhead concept, common components were aligned in specific planes through the system. As an example, shown below in Figure 11, the water vapor channel focus optics were positioned in plane with the focus elements of the gas cell channels. This facilitated the bulkhead concept.

Figure 11: Forward Optical Payload Structure
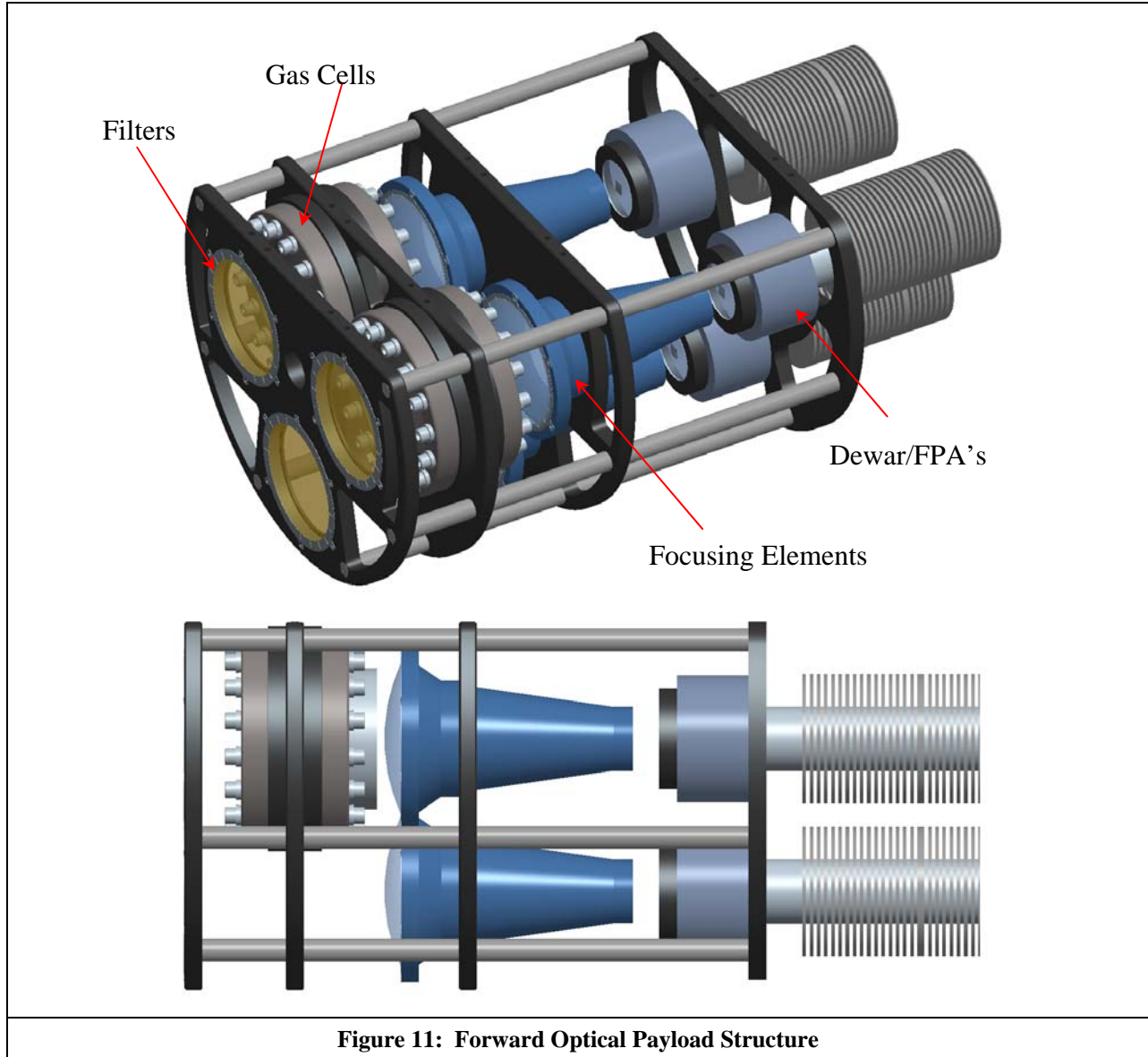
The filter bulkhead houses three filters, one for each channel. Each optic sits within a pocket, with an axial preload applied by the flexure rings to retain it in place. To control centration within the bulkhead, thermal bumpers can be injected into the pocket sides, which would bond to the optic and bulkhead pocket. The thermal bumpers are an adhesive with a very low modulus, which makes them very soft and forgiving for differential CTE's between the bulkhead and glass materials. The bulkhead can be light-weighted to further weight reduction. Structural analysis will need to be performed to find the optimal weight to stiffness design for all bulkheads.
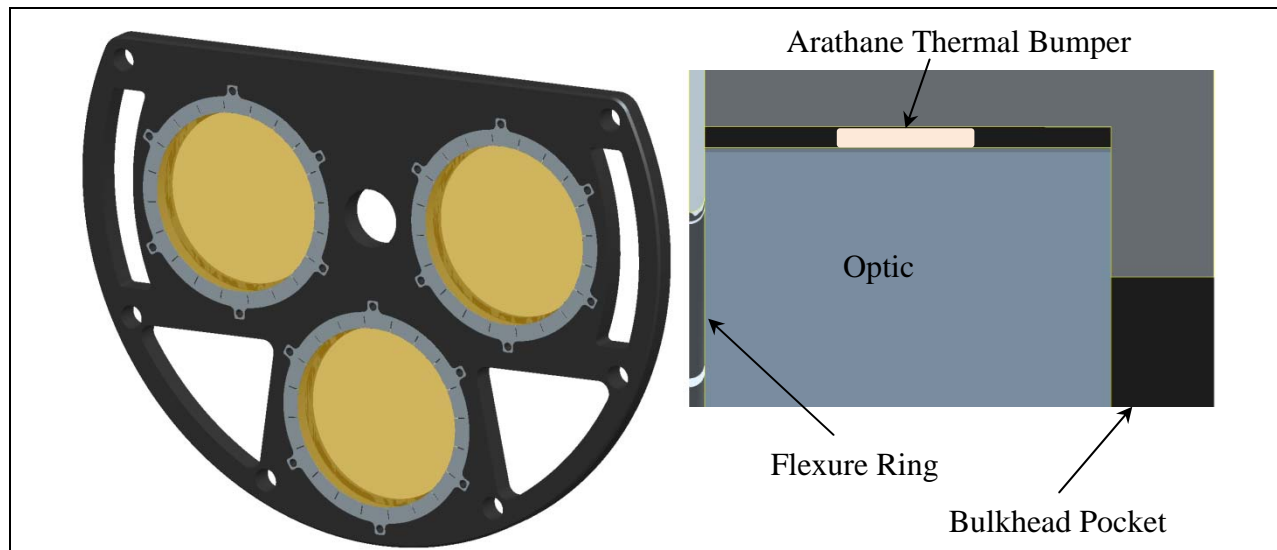
Figure 12: Filter Bulkhead

For the gas cells, both are housed in a gas cell bulkhead. The gas cells attach to the bulkhead via radially spaced fasteners. The sleeve in which the gas cell inserts into the bulkhead controls tip/tilt positioning by mechanical tolerances. Appropriate clearance must be made to allow access for gas cell refill plumbing (not shown). As a further design iteration, access features in the bulkhead could be added to allow for easy swap of the gas cells in and out of the bulkhead, if necessary. In addition to the gas cell mounts, the bulkhead contains a third port for beam clearance to prevent light clipping for the water vapor channel.
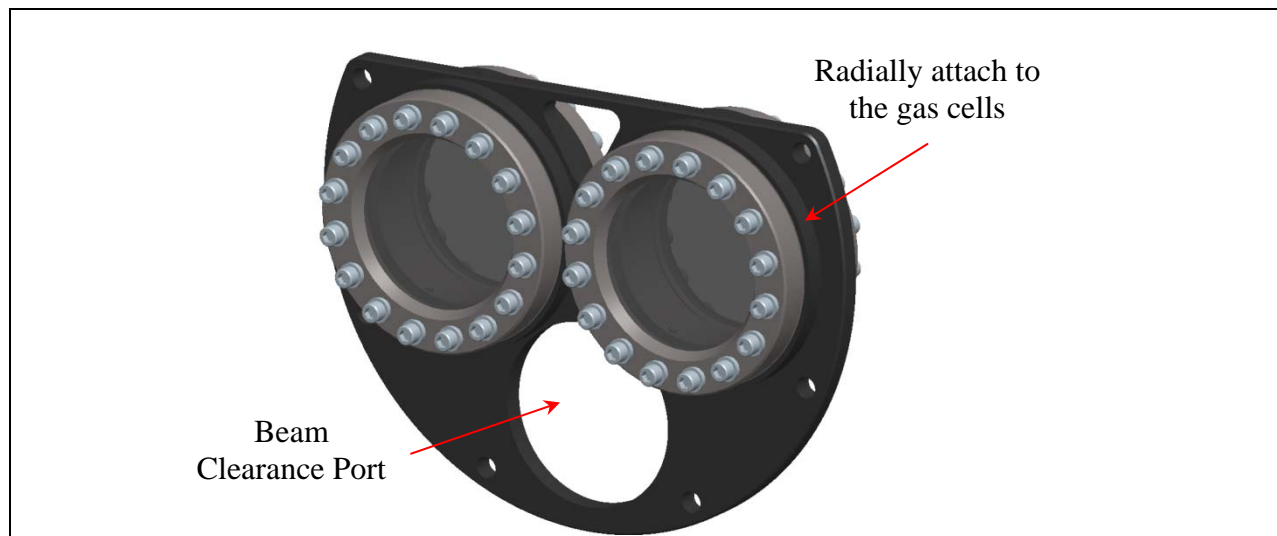
Figure 13: Gas Cell Bulkhead

The next bulkhead is the focus element bulkhead. Since the focus elements tend to have tighter tolerances, relative to each other, these optics were designed to be aligned to a separate sub-cell. This allows the focus elements to be aligned, relative to each other, within a much higher fidelity part than the system bulkheads would allow. As with the filters, the front two elements are axially held in with a flexure ring. The piston placement is controlled by housing tolerances and

24

a spacer. The spacer directly controls piston between the first and second element, while the positional tolerance of the second elements shelf mount will ultimately place the piston location of the third element. As with the filters, centration is controlled with thermal bumpers. The third optic will be actively aligned and structurally bonded into radial flexures. This will allow the third optic to compensate for tolerance stack up error of the first two elements, while still accommodating the thermal and mechanical environments. Once aligned to their respective housings, the focus element housing assembly is assembled and fastened onto the bulkhead. The housing assemblies attach to the bulkhead at their center of gravity to reduce tip/tilt induced into the system through environments. To control tip/tilt between the housing and the bulkhead during mounting, the mounting features/location should be adequately controlled such that tolerances are within acceptable range to meet alignment tolerances.
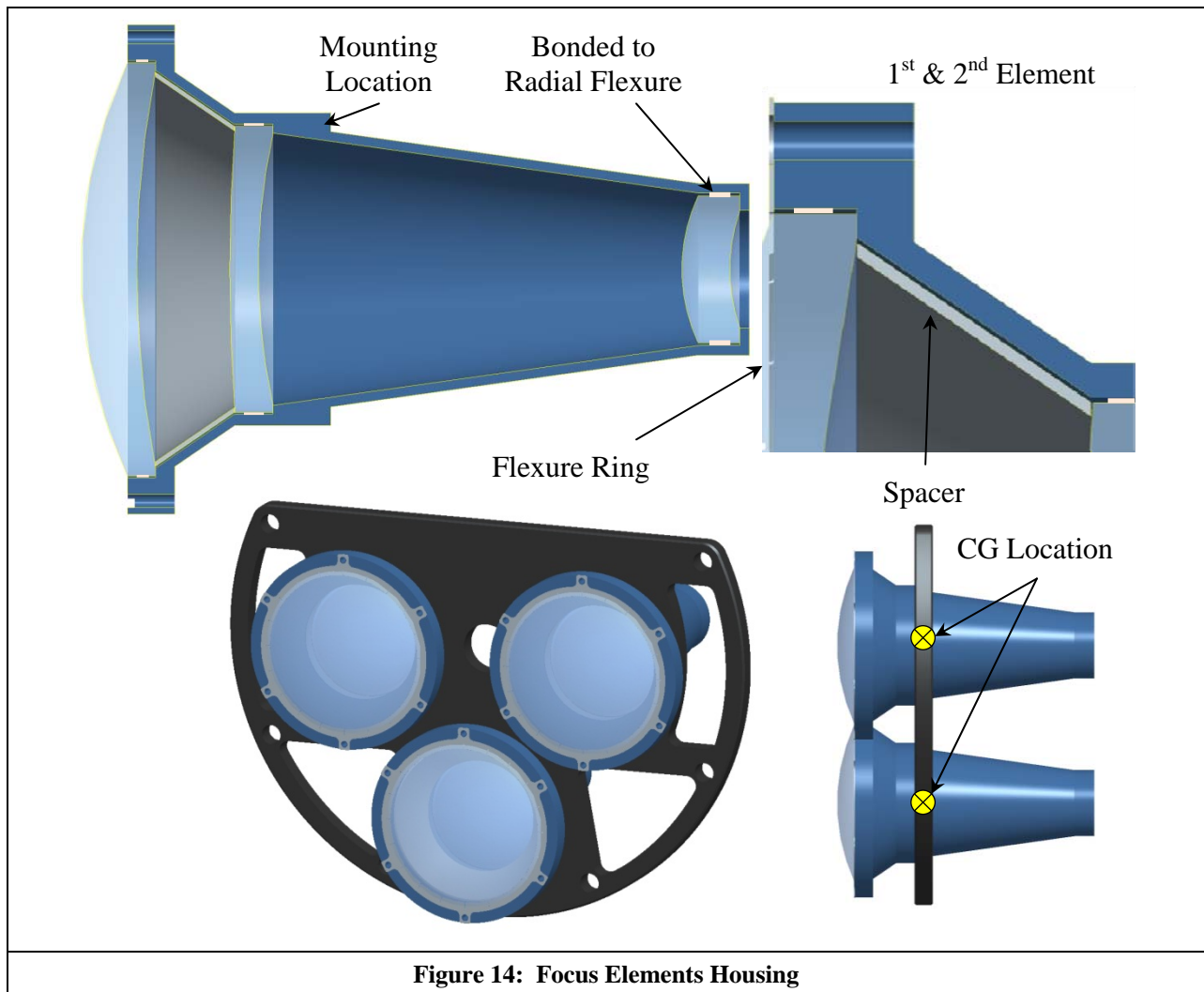
Figure 14: Focus Elements Housing

The dewars are also mounted separately into their own bulkhead mount. For this concept a closed cycle dewar was selected, which is commercially available, to house the FPA's. These dewars have an agreeable form factor for the pod configuration. To mount the dewars, they are inserted into the bulkhead mount, and moved into position to bolt onto the attachment points. A secondary structure (not shown) is necessary to mount the FPA electronics, dewar pumps, etc, but would ideally be placed immediately behind the FPA bulkhead.

Insert dewer through clearance hole, and slide into slotted position.
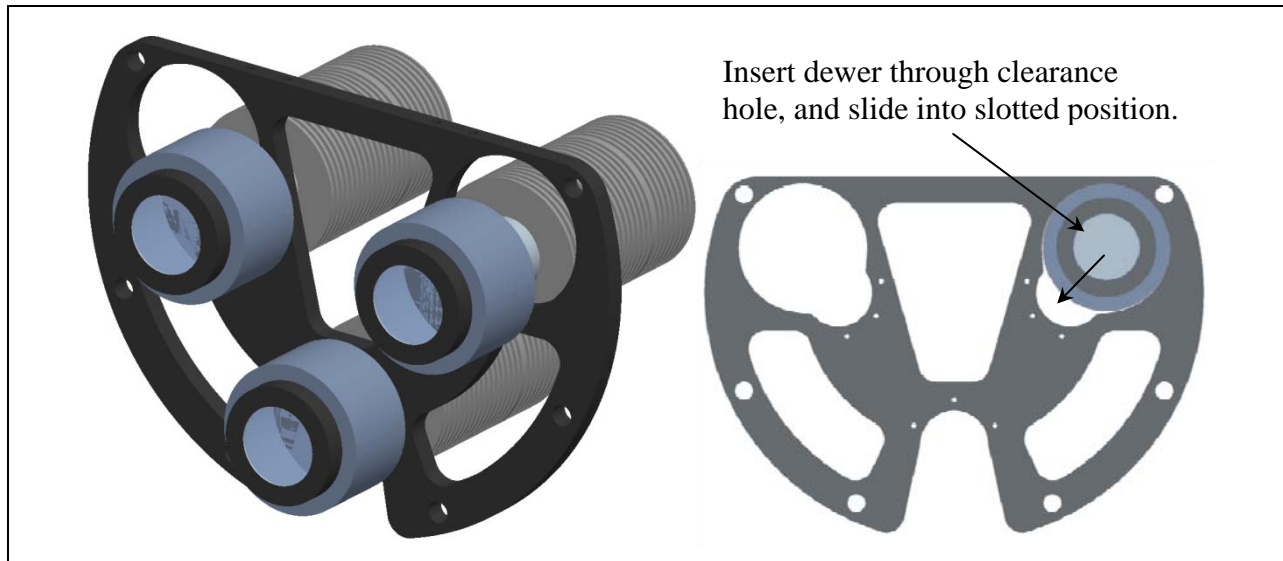
Figure 15: Closed Cycle Dewars

Once all subcomponents have been assembled into their respective bulkheads, they can then be aligned and assembled together to create the forward optical payload. To assemble this payload, structural/metering rods are used to connect each section. In addition to structural support, these rods can control piston and centration. Due to their cylindrical nature, they can be machined to tight tolerances for relatively inexpensive cost, if necessary.

Structural/Metering Rods
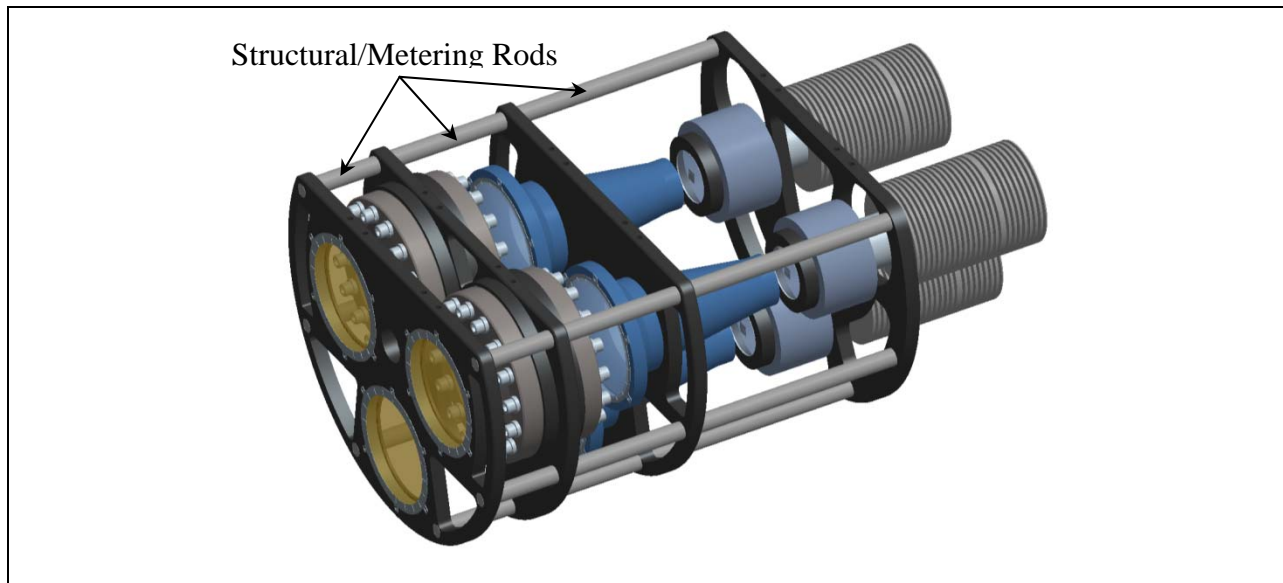
Figure 16: Forward Optical Payload Assembly

To attach the forward optical payload to the pod backbone structure, an interface plate is installed. This interface plate connects to each of the bulkheads previously discussed in addition to the pod backbone, via fasteners. This further strengthens the optical payload structure to become more rigid.

Bulkhead Mounting Locations

Pod Backbone Mounting Locations
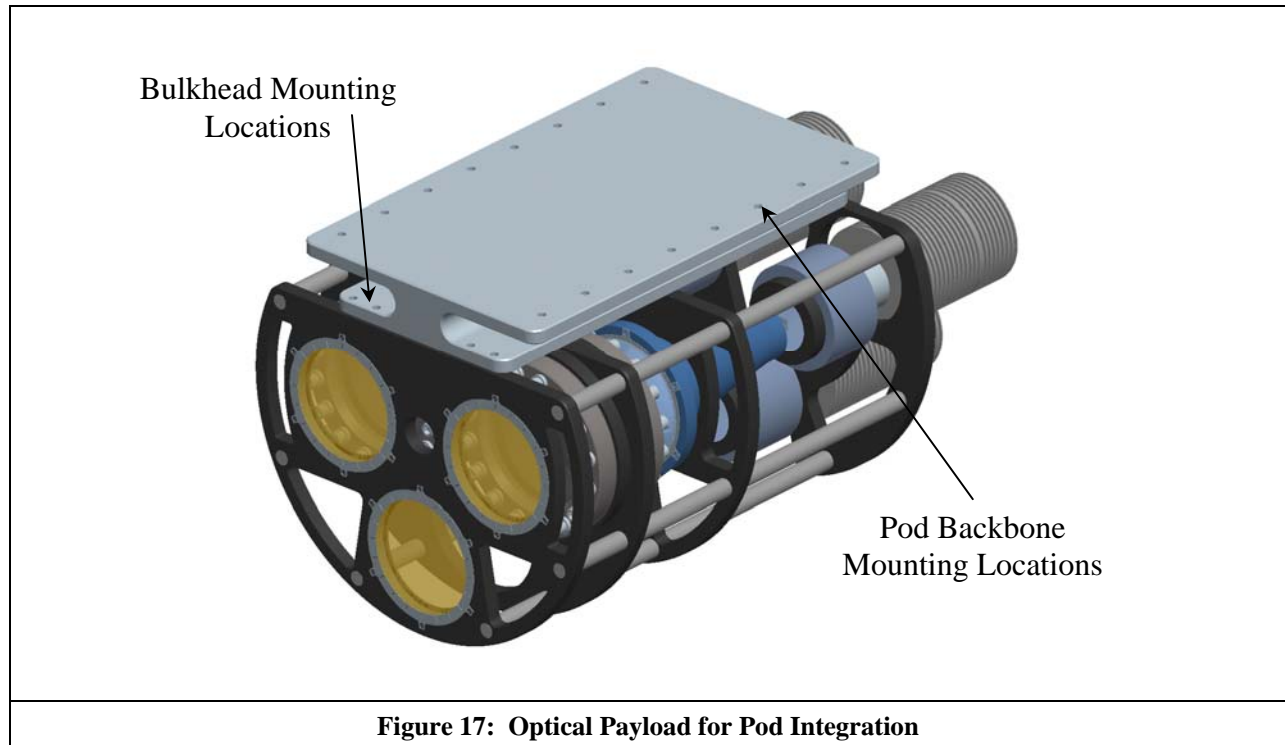
Figure 17: Optical Payload for Pod Integration

3.2.2.1 Rear Gimbal

As previously mentioned, the second payload is the rear gimbal. The rear gimbal is a nested two axis gimbal. Along with the forward looking angle discussed earlier, the side angle is ±5°. This angle is limited primarily due to the window width, shown in Figure 19 below. Increasing the width will increase the side angle, but will also increase the amount of stray light entering the system. Due to this effect, further stray light mitigation design would need to be done (such as baffling) to optimize the system performance. Due to the size constraints, this gimbal will need to be a custom part. However, Org-05343 has significant experience designing custom gimbals, and this experience would be leveraged in the design of this system. The size of this gimbal is driven by the size of the mirror. In the current concept, the mirror must be at least 10.5 inches in diameter to not vignette/clip light into the channels at steep angles. However, this size increases the larger the pointing angle is. This implies looking straight down (i.e. mirror at 45 deg) increases the required mirror size to 14.85 inches in diameter.

=10.5 in
Diameter
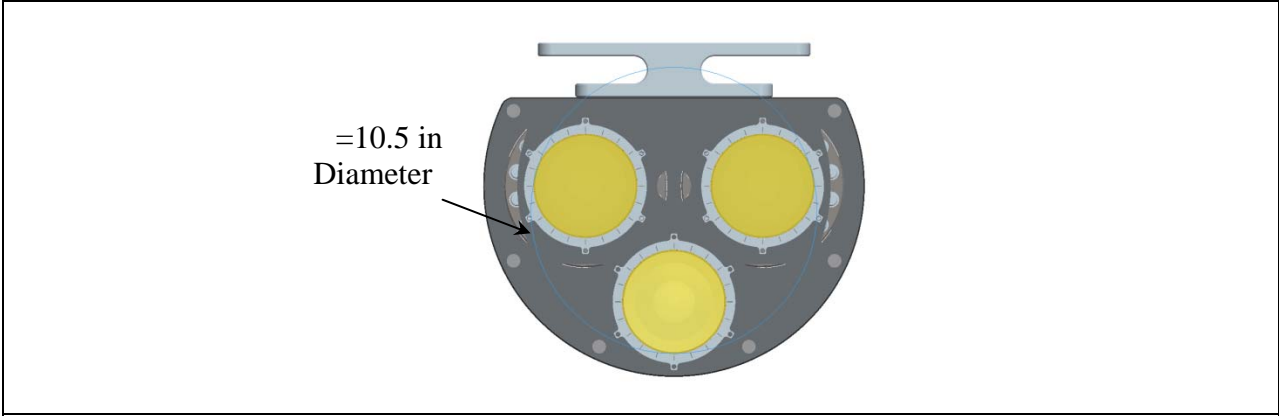
Figure 18: Minimum Mirror Size

Side Viewing
Angle

5°

Top View

Bottom View

Window size
(width) limits side
view angle

Figure 19: Gimbal Side Viewing Angle

4. PERFORMANCE PREDICTIONS

4.1. Satellite measurements of CH_4 column

The performance predictions that are presented in this section were made using the column perturbation model. This model assumes that CH_4 is distributed throughout the atmosphere according to a prescribed profile of concentration as a function of altitude. The concentration at all altitudes is then scaled by a constant ratio. The next sections describe the inputs to this model and the performance that was predicted for a satellite sensor that would make global measurements of the total column amount of CH_4 in the atmosphere for the purpose of greenhouse gas monitoring and studies.

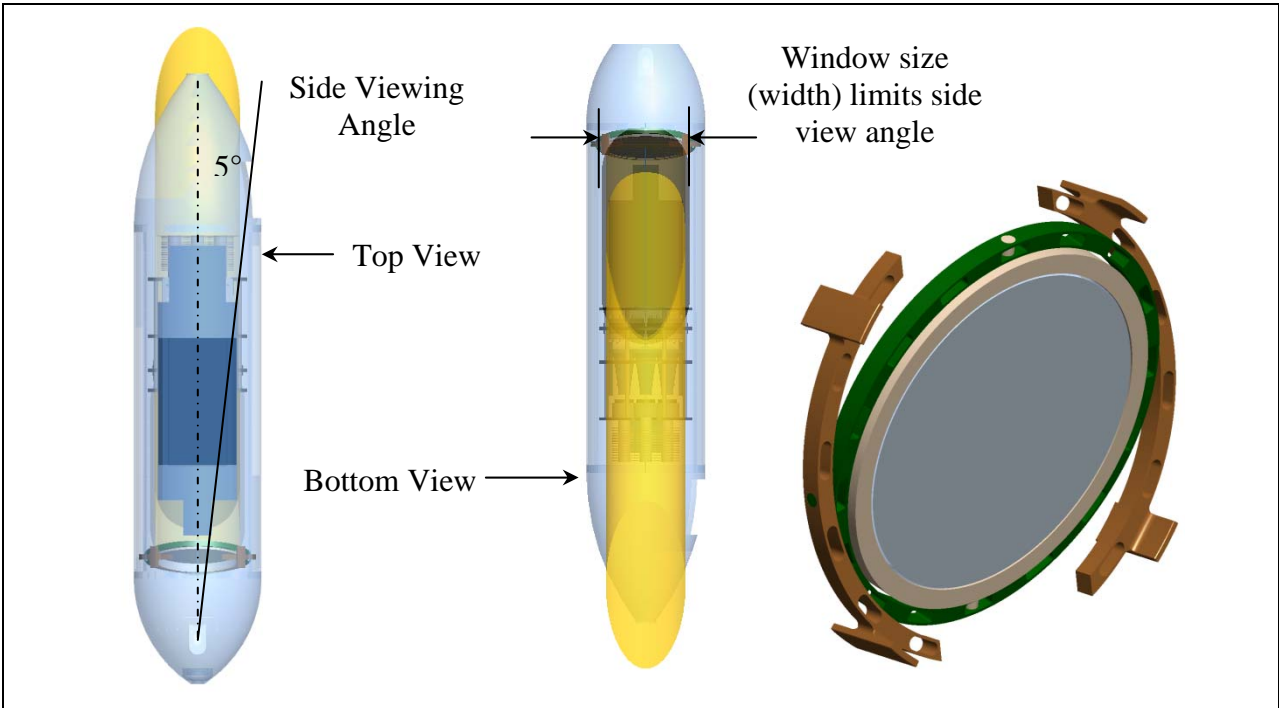### 4.1.1. Scene assumptions

Absorption of solar radiation during propagation through the atmosphere was calculated using the SAMM2 line-by-line code from Spectral Sciences, Inc. using the profiles prescribed by the U.S. 76 standard atmosphere. The results of the calculations were collected into three types of output files. One type of file includes absorption only by CH_4, so that the effect of changing the CH_4 column could be studied. The second type of file includes absorption only by H_2O, which has strong absorption features in the same spectral regions as the CH_4 line and whose distribution is highly variable as a function of geographical location and time of year. The third type of file includes absorption by all other molecular species defined in the U.S. 76 standard atmosphere. The third file represents a more or less fixed background of absorption features due to a large variety of molecular species, including CO_2, O_3, N_2O, CO, NO, SO_2, NO_2, NH_3, HNO_3, and OH. All calculations were run for a 45° solar zenith angle for a path that ran from the top of the atmosphere down to sea level. The model then adjusted the transmission for other solar zenith angles and for a return path to the sensor.

The surface of the earth was treated as a Lambertian scattering surface. Tabulated data that was extracted from MODTRAN was used to set surface albedo as a function of wavelength. The radiometric model calculates the signal from only a single pixel of specified albedo. Surface emissivity was set to one minus the albedo. Surface temperature was set to 35 ^{o}C for the purpose of calculating thermal radiation emitted by the earth.

4.1.2. Sensor assumptions

The assumptions made about the sensor are presented in three groups. The first group is a set of fixed optical design parameters. The second group is a set of detector parameters. Detector performance is a key element in determining overall system performance and so we ran calculations for three types of detectors: an ideal (i.e. noise free) detector, an expensive custom detector with close to idea performance, and a much less expensive off-the-shelf detector with notably higher noise levels and hence significantly reduced performance. The first group is a set of fixed optical design parameters. The second group is a set of detector parameters.

Table 3: Sensor optical parameters for CH_4 total column measurements.		
Parameter	**Value**	**Units**
Effective focal length	32	cm
Diameter of entrance pupil	16	cm
Diameter of central obscuration	5.3	cm
General optics temperature	25	degrees C
Sensor interior temperature	25	degrees C
Peak transmission	0.375	dimensionless
Short pass 95% wavelength	2.5	µm
Short pass 5% wavelength	2.7	µm
Out-of-band blocking	0.0005	dimensionless
Bandpass center wavelength	2.275	µm
Bandpass full width at half maximum	0.085	µm
Length of gas cells	5.0	cm

Table 3 lists the sensor optical parameters. The diameter of the entrance pupil was set to match the value of the Orbiting Carbon Observatory (OCO). The effective focal length produces a relatively fast F/2 system. The diameter of the central obscuration was set to a conservative value of 1/3 of the entrance pupil diameter. The temperature of the optics and the rest of the interior of the sensor were set to standard room temperature values. Size and weight are important constraints for a spaced based sensor, and so it was assumed that the gas and reference channels would share a common set of collecting optics, and that a beam splitter would be used to divide the light between the two channels. The peak transmission of 0.375 includes the effect of a 50/50 beam splitter.

Table 4: Detector parameters for CH_4 total column measurements.			
Parameter	**Ideal Detector**	**Custom Detector**	**Off-the-Shelf**
Quantum efficiency	0.95	0.95	0.75
Pixel height (µm)	450	450	450
Pixel width (µm)	450	450	450
Dark current (e^- s^{-1} $pixel^{-1}$)	0	3.7e5	2.6e10
Read or reset noise (e^- $pixel^{-1}$)	0	405	9000
Full well capacity (e^- $pixel^{-1}$)	7.0e8	6.2e8	7.9e8
Maximum integration time (s)	10	1	1

Table 4 lists the three sets of detector parameters that were used for the performance predictions. Predictions made using an ideal detector (i.e., a detector that adds zero noise) show the fundamental performance limits for the optical parameters listed in Table 3 and the platform parameters listed in Table 5. Predictions made using the custom detector parameters show how

closely this limit can be approached using a real, but customized and therefore expensive, detector array. Predictions made using the off-the-shelf parameters show the degradation that would result from using a cheaper, readily available detector. In practice a satellite sensor would probably be designed around a custom detector. The pixel height and width were set to produce a ground instantaneous field-of-view (GIFOV) of approximately 1 km on a side given the effective focal length listed in Table 1 and the orbital altitude listed in Table 3. The resulting dimensions of 450 µm on a side are very large compared to typical pixel dimensions of 20 to 30 µm on a side. The calculations were based on the assumption that individual pixels that would be summed together to produce the desired spatial resolution. Some quantities, such as effective full well capacity and total dark current, scale in direct proportion to the total number of pixels summed. Other quantities, such as read noise, scale as the square root of the number of individual pixels summed.

Table 5: Geometrical parameters for CH_4 total column observations.		
Parameter	**Value**	**Units**
Orbital altitude	705	km
Sensor look angle	25	degrees
Solar zenith angle	45	degrees
Ground IFOV	1	km

Table 5 lists a few key parameters that are related to the platform and viewing geometry. The orbital altitude was set to match what was planned for the Orbiting Carbon Observatory (OCO) and the optical and detector parameters listed in Tables 3 and 4 were adjusted to produce the same ground IFOV as planned for the OCO. The OCO sensor was highly optimized to measure major carbon containing greenhouse gases in the earth's atmosphere, but unfortunately the payload failed to reach orbit. OCO did not use the gas correlation method, but it makes sense to mimic the altitude and ground IFOV since these were chosen by NASA after extensive science based trade studies.

4.1.3. Performance predictions

Figure 20 shows the performance predictions that were made using the input parameters listed in Tables 3-5. The horizontal axis shows the total data collection time, which is the amount of time the sensor would stare at a given field-of-regard. Multiple detector readouts would be required for data collection times that exceed the maximum allowed integration time listed in Table 4. The vertical axis shows the signal-to-noise ratio (SNR) that would be produced as a function of total data collection time when measuring a fairly small 0.1% change in the CH_4 total column amount. The heavy black line corresponds to an SNR of 3, which is a simple, general performance goal. The sloped lines of various colors show the performance for the different detectors listed in Table 4. The line for the custom detector very nearly overlaps the line for the ideal (zero noise) detector. This indicates that the noise introduced by the custom detector is negligible compared to the shot noise of the solar signal and thermal background.

Figure 20: Performance predictions for CH$_4$ total column measurements.
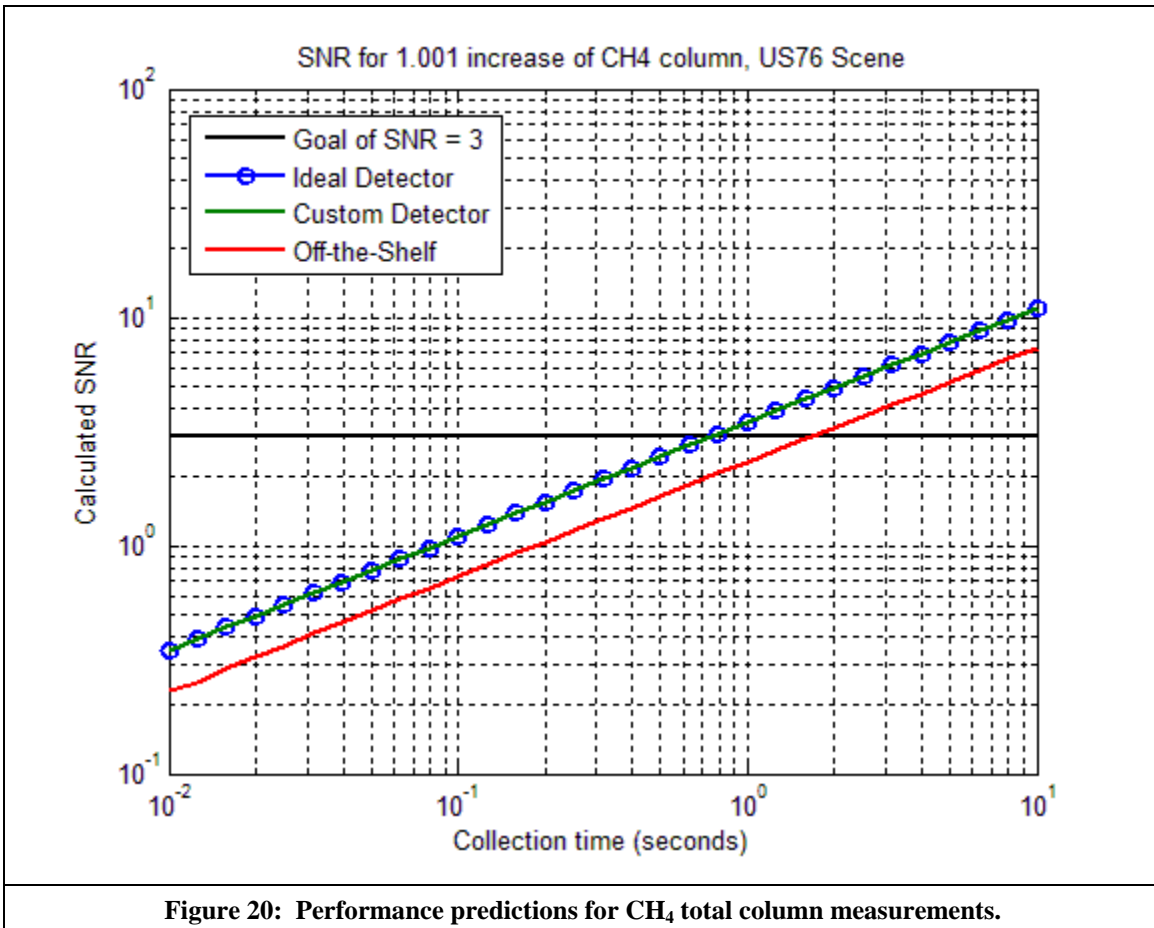
The line plotted for the custom detector in Figure 20 shows truly excellent performance – a 0.1% change in CH$_4$ total column could be detected in slightly less than 1 second of observation time using a sensor with a modest 16 cm diameter entrance pupil. This indicates the power of the gas filter correlation technique in a case when the gas of interest has characteristics (i.e. low concentration in the atmosphere and strong optical absorption) that are well matched to the gas filter correlation measurement technique.

4.1.4 Sensor Motion Noise Modeling

When modeling system performance, platform motion can be a major noise source. The noise is characterized as clutter equivalent irradiance or a clutter equivalent target (CET). To estimate CET, first simulated background imagery is generated in the spectral bands of interest. The noise is then estimated by using a Monte Carlo simulation of the temporal pixel radiance fluctuations caused by scene motion. Under this effort, a preliminary evaluation of scene clutter for the space-based CH$_4$ system design described above has been completed. A complicated scene including agriculture, ocean, mountains and urban areas was chosen to provide a diverse background. The simulated image for the conceptual sensor in the CH$_4$ band can be seen below in Figure 21. The scene simulation package used for this work was the PRA Toolkit.

Figure 21: Simluated space based image in the 2.7 μm CH$_4$ band

Since a specific platform for the space based implementation has not been chosen, a conservative value for platform stability has been selected at 3 micro radians mean RMS jitter per axis. Assuming the integration time is set to 10 ms allows for a 100 scans per second to be collected, The SNR can be improved by summing scans into frames. The number of scans summed multiplied by the integration time is identified as the total data collection time. The noise generated due to this platform motion as a function of data collection time for these conditions can be seen below in Figure 22.
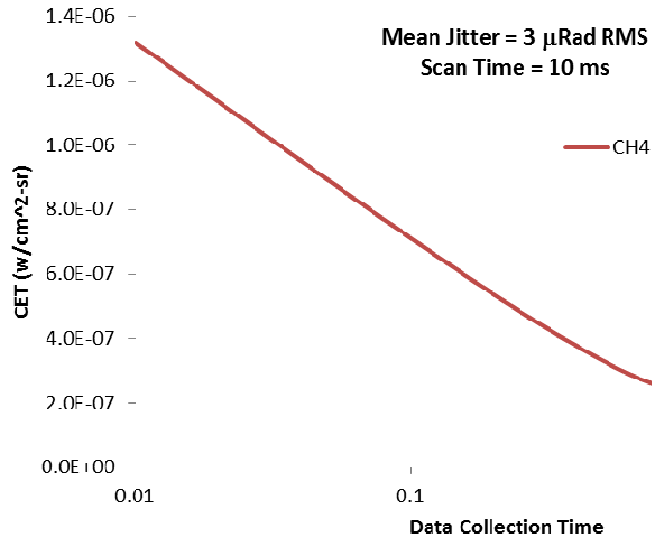
Figure 22: Clutter radiance vs. data collection time for space based CH4 sensor

The noise induced by the platform motion can then be used to identify what data collection time is required to fall below the desired minimum detectable quantity. The tools used to simulate these effects will prove to be useful in the case that a system design for a space based platform is realized. Running a simulation like the one shown above for different platform motion amounts will provide the required image stabilization level that is necessary to meet the desired mission.

4.2. Three Dimensional Plume Simulations

A considerable amount of time and effort went in to creating detailed modeling capabilities for the simulation of chemical plume effluent transport. The motivation for this portion of the research is to apply advances in computational fluid dynamics, visualization, and data processing for the analysis of plume dispersal. The goal is to better understand aerosol dispersal behavior as it relates to remote sensing and data interpretation. To achieve this goal, several Fuego aerosol dispersion models that released various gases from a stack under a cross wind have been developed. The Boussinesq buoyancy model, and the dynamic Smagorinsky and time-filtered Navier Stokes turbulence models were primarily used for this effort. Fuego is a mature, massively parallel CFD code that addresses plume transport and mixing at a far finer scale and with far more detail than any existing Gaussian or puff-based transport models. Fuego is a 3D, incompressible (low Mach), reactive flow, massively parallel, generalized unstructured code that includes:

- Laminar, buoyancy, and turbulent flow models
- Convective operators with flux limiters
- Combustion models
- Participating media radiation
- Conjugate heat transfer

Because of the amount of detail involved in CFD modeling effort, an entirely separate 2012 SAND report, "Stack Aerosol Modeling under Various Release Rates and Wind Conditions"; by S. Rodriguez & J. Mercier has be published. That report contains all of the modeling theory along with the details of the model inputs and output.

The model typically consisted of a stack at a given location that was discharging aerosols at a given stack velocity and under a wind cross-flow as shown below in Figure 23.
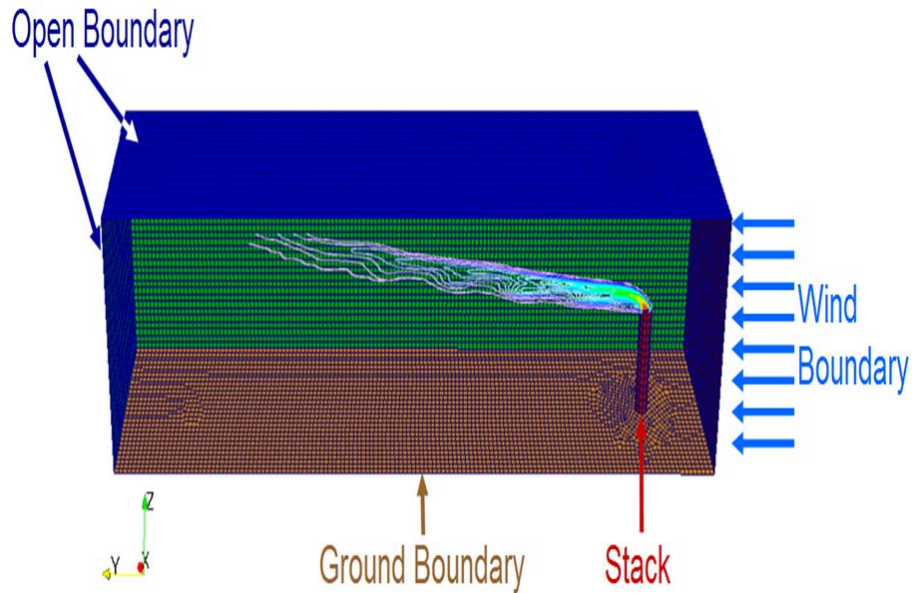
Figure 23: Plume dispersion model

The Fuego model outputs the temperature, pressure and concentration of the plume species at every mesh point. The plumes are read into the ParaView software, which is an open-source, multi-platform data analysis and visualization application, and each time step is written out as a Excel CSV file. Each line in the file corresponds to the values of pressure, density, temperature, x-velocity, y-velocity, z- velocity, and concentration of the species in a particular cell of the simulated flow. The CSV files are then read into a MATLAB code which is used to determine lines-of-sight (LOS) through the plume and solves the radiative transport (RT) equation along each LOS to generate the transmission and emission from the flow along the LOSs. The LOS generation is illustrated in Figure 24. The properties along a given LOS are broken into short homogeneous segments whose properties are derived from interpolation of the flow field and atmospheric properties. The MATLAB tool provides an option to visualize the position of the sensor relative to the plume and the user selected ensemble of LOSs. This feature was used to create Figure 24.
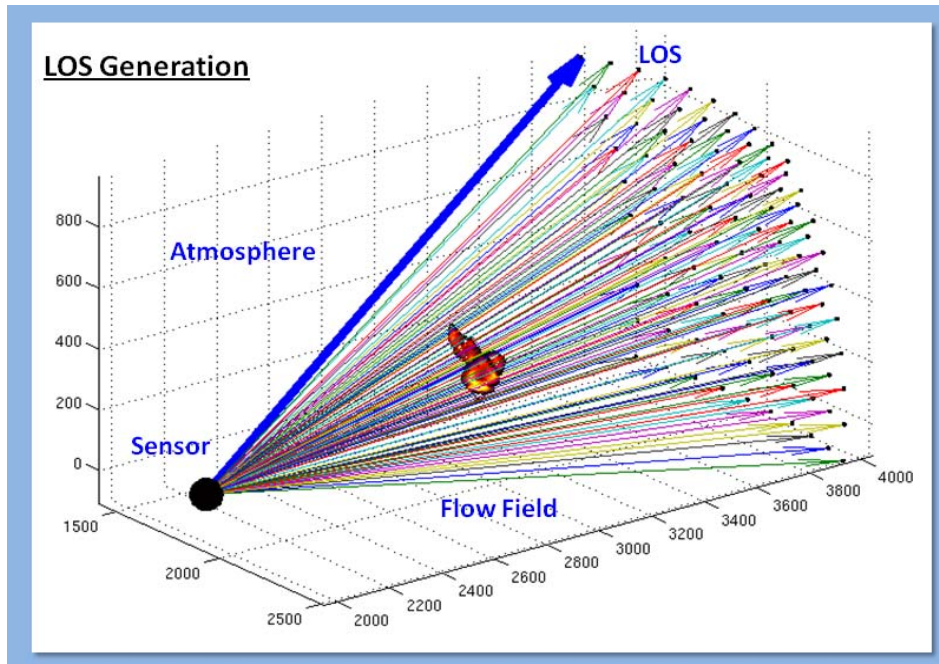
Figure 24: Visualization of plume, sensor and LOS with Matlab tool

The output properties are the 2D integrated transmission and emission for the user selected field-of-view (FOV). These outputs are generated using the line-by-line solution to the radiative transfer equation in the code SAMM2. SAMM-2 is the state-of-the-art in all-altitude radiative transport code developed for the Air Force Research Laboratory. A representative 2D radiance map is shown below in Figure 25.
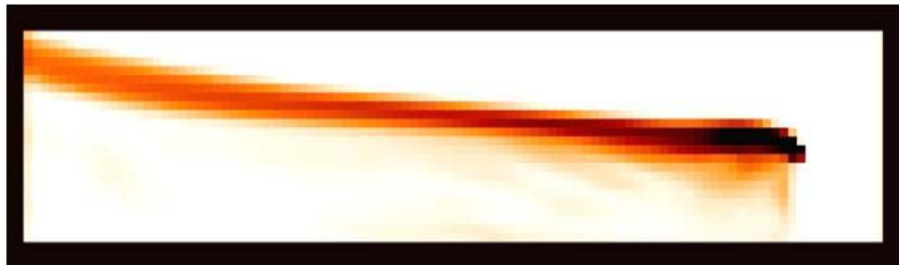
Figure 25: Plume transmission plot for CH4 at 2.27 μm

SAMM-2 combines the capabilities of two older Air Force Research Laboratory codes into a single all-altitude radiance and transmission code. The first of these codes is MODTRAN. MODTRAN is a well-established standard for lower atmosphere (altitudes below 50 km) computations. Physically, the lower atmosphere is characterized by molecular dynamics dominated by collisions. Local temperatures in this local thermodynamic equilibrium (LTE) regime are well-defined and molecular excited state populations follow the Planck function. This is in marked contrast to the physical characteristics of the upper atmosphere (altitudes above 40 km). The lower molecular densities of the upper atmosphere makes spontaneous emission and not molecular collisions the dominant excited state relaxation process. In this non-local thermodynamic equilibrium (NLTE) regime, the concept of a single local temperature is no longer meaningful and internal molecular state concentrations need to be explicitly computed as radiance sources. For these cases, the Standard High-Altitude Radiance Code (SHARC) is

applicable. SAMM-2 retains the vast majority of the capabilities of these two older codes. One significant divergence is the choice of RT algorithms. In order to unify the RT treatment, SAMM-2 replaces the single-line-equivalent-width algorithm in SHARC and the band model algorithm in MODTRAN with a single high-fidelity LBL RT algorithm (QBL) capable of predicting spectral radiances with a 0.001 cm-1 resolution. It is this LBL capability that makes SAMM-2 useful for modeling gas plumes at the high spectral resolution that is required under this effort.

4.3. Airborne measurements of CH_4 plumes

The performance predictions that are presented in this section were made using the plume perturbation model. This model assumes that a standard background of CH_4 is distributed throughout the atmosphere according to a prescribed profile of concentration as a function of altitude. A plume of specified product of concentration $\times$ path length is then inserted into the field-of-view of the sensor. The next sections describe the inputs to this model and the performance that was predicted for an airborne sensor that would measure plumes of CH_4. A likely application would be monitoring natural gas pipelines for leaks.

4.3.1. Scene assumptions

The assumptions for the background (unperturbed) scene were essentially the same as those described in section 4.1.1 for satellite measurements of CH_4 column. A plume of CH_4 was then added to perturb the scene. The transmission of the plume was calculated using the same SAMM2 line-by-line code used to calculate transmission of the unperturbed atmosphere. However, the plume was assumed to be at a fixed pressure of 1 atmosphere and at a fixed temperature of 30 ^oC. The plume temperature was set to be consistent with the 35 ^oC temperature specified for the underlying surface of the earth. The temperatures were set to relatively high values in order to create a conservative (i.e. higher than typical) level of thermal background radiation.

4.3.2. Sensor assumptions

The assumptions made about the airborne sensor will be presented in three groups, just as they were for the satellite sensor. The first group is a set of fixed optical design parameters. The second group is a set of detector parameters. The first group is a set of fixed optical design parameters. The second group is a set of detector parameters.

Table 6: Sensor optical parameters for CH$_4$ plume measurements.		
Parameter	**Value**	**Units**
Effective focal length	15	cm
Diameter of entrance pupil	7.5	cm
Diameter of central obscuration	0	cm
General optics temperature	25	degrees C
Sensor interior temperature	25	degrees C
Peak transmission	0.75	dimensionless
Short pass 95% wavelength	2.5	micrometers
Short pass 5% wavelength	2.7	micrometers
Out-of-band blocking	0.0005	dimensionless
Bandpass center wavelength	2.275	micrometers
Bandpass full width at half maximum	0.085	micrometers
Length of gas cells	5.0	cm

Table 6 lists the sensor optical parameters. The diameter of the entrance pupil and the effective focal length were set based on the design described in section 3. The value of 0 for the diameter of the central obscuration is appropriate for a design that uses only refractive elements. The temperature of the optics and the rest of the interior of the sensor were set to standard room temperature values. The peak transmission of 0.75 is twice as large as the value shown in Table 1 for the satellite sensor because the airborne sensor will use independent optics for the two channels, rather than using a beam splitter to divide the light from a single aperture.

Table 7: Detector parameters for CH$_4$ plume measurements.			
Parameter	**Ideal Detector**	**Custom Detector**	**Off-the-Shelf**
Quantum efficiency	0.95	0.95	0.75
Pixel height (µm)	100	100	100
Pixel width (µm)	100	100	100
Dark current (e$^-$ s^{-1} pixel^{-1})	0	1.8e4	1.3e9
Read or reset noise (e$^-$ pixel^{-1})	0	89	1980
Full well capacity (e$^-$ pixel^{-1})	3.0e7	3.0e7	3.8e7
Maximum integration time (s)	10	1	1

Table 7 lists the three sets of detector parameters that were used for the performance predictions. Predictions made using an ideal detector (i.e., a detector that adds zero noise) show the fundamental performance limits for the fixed optical parameters listed in Table 6 and the fixed platform parameters listed in Table 8. Predictions made using the custom detector parameters show how closely this limit can be approached using a real, but customized and therefore expensive, detector array. Predictions made using the off-the-shelf parameters show the

degradation that would result from using a cheaper, readily available detector. The pixel height and width were set to produce a ground instantaneous field-of-view (GIFOV) of approximately 2 meters on a side given the effective focal length listed in Table 6 and the flight altitude listed in Table 8.

Table 8: Platform parameters for CH_4 plume measurements.		
Parameter	**Value**	**Units**
Flight altitude	3	km
Sensor look angle	0	degrees
Solar zenith angle	45	degrees
Ground IFOV	2.0	meters

Table 8 lists a few key platform parameters that are related to the platform and viewing geometry. The flight altitude was set to a value that would be convenient but that is not tied to a specific concept of operations. The solar zenith angle is 45°, just as for the satellite measurements of CH_4 column. However, the sensor look angle was set to 0° on the assumption that an aircraft would fly straight overhead when inspecting a natural gas pipeline for leaks.

4.3.3. Performance predictions

Figure 6 shows the performance predictions that were made using the input parameters listed in Tables 6-8. The horizontal axis shows the total data collection time, which is the amount of time the sensor would stare at a given field-of-regard. Multiple detector readouts would be required for data collection times that exceed the maximum allowed integration time listed in Table 7. The vertical axis shows the signal-to-noise ratio (SNR) that would be produced as a function of total data collection time when measuring a plume with a concentration × path length product of 100 ppm-meters. The heavy black line corresponds to an SNR of 3, which is a simple, general performance goal. The sloped lines of various colors show the performance for the different detectors listed in Table 7. The line for the custom detector again overlaps the line for the ideal (zero noise) detector. This indicates that the noise introduced by the custom detector is negligible compared to the shot noise of the solar signal and thermal background.
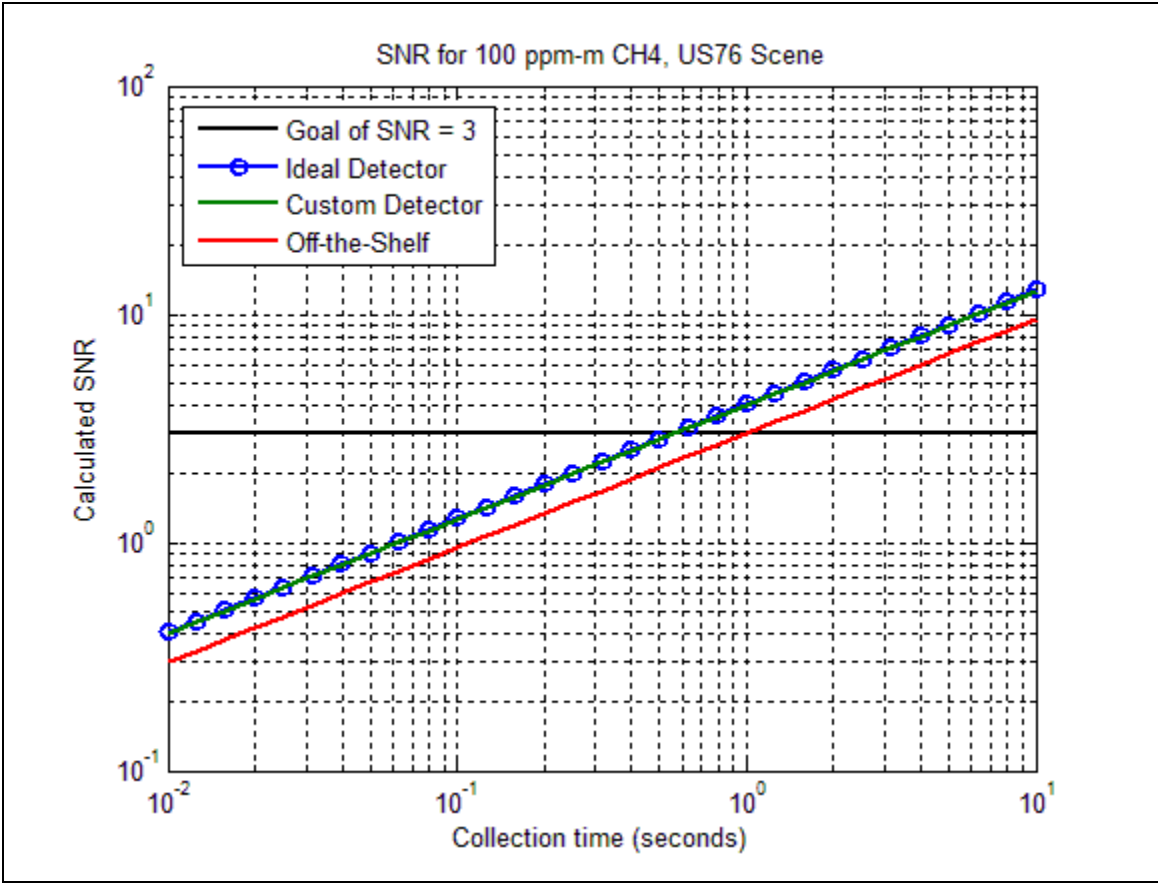
Figure 26: Performance predictions for CH₄ plume measurements.

5. CONCLUSIONS

The purpose of the project was to investigate gas filter correlation radiometry as a technique for optical remote sensing of a suite of gases that are of special interest for Sandia's Remote Sensing and Verification Program. The primary goals of this work were to build a model for radiometric calculations and to use that model to predict sensor performance for conceptual airborne and space-based gas filter correlation radiometers. All of the major goal of this R&D effort have been accomplished and there now exists a unique capability to model effluents and predict GFC sensor design concept performance against those effluents. The tools and models developed under this work will be critical for the design trades that need to be made for any future GFC sensor work that is done at Sandia.

6. REFERENCES

1. R. W. Boyd, *Radiometry and the detection of optical radiaion*, John Wiley and Sons, New York, NY (1983), ISBN 0-471-86188-X.

2. H. Edner, S. Svanberg, L. Unéus, W. Wendt, "Gas-correlation lidar," *Opt. Lett.*, Vol. 9, pp. 493-495, (1984).

3. J.T. Houghton and S.D. Smith, "Remote Sounding of Atmospheric Temperatures from Satellites. I. Introduction," *Proc. Roy. Soc. London, Series A*, Vol. 320, pp. 23-33 (1970).

4. E. Galletti, E. Zanzottera, S. Draghi, M. Garbi, and R. Petroni, "Gas correlation lidar for methane detection, " *Proceedings NASA Langley Research Center 13th International Laser Radar Conference* (Aug., 1986).

5. J. C. Gille, L. Pan, M. W. Smith, P. L. Bailey, and D. P. Edwards, "Retrieval of profiles of carbon monoxide and total methane columns from MOPITT measurements," *Proc. AGU*, (Dec., 1994).

6. L. Pan, D. P. Edwards, J. C. Gille, M. W. Smith, and J. R. Drummond, "Satellite remote sensing of tropospheric CO and CH4: forward model studies of the MOPITT instrument, " *Appl. Opt.*, Vol. 34, pp. 6976-6988 (Oct. 1995).

7. S.B. Rodriquez and J. A. Mercier "Stack Aerosol Modeling Under Various Release Rates and Wind Conditions — Parametric and Visualization Analysis Overview" SAND Report 2012.

8. J. M. Russell, III, J. H. Park, and S. R. Drayson, "Global monitoring of stratospheric halogen compounds from a satellite using gas filter spectroscopy in the solar occulation mode," *Appl. Opt.*, Vol. 16, pp. 607-612 (1977).

9. J. M. Russell, III, L. L. Gordley, J. H. Park, S. R. Drayson, W. D. Hesketh, R. J. Cicerone, A. F. Tuck, J. E. Frederick, J. E. Harries, and P. J. Crutzen, "The halogen occultation experiment," *J. Geophys. Res.*, Vol. 98, pp. 10,777-10,797 (1993).

10. M.W. Smith and S. R. Shertz, "Current plans and status of MOPITT Algorithm Test Radiometer (MATR)," *Proc. SPIE* ,Vol. 2820, pp. 78-86, Aug. 1996.

11. M.W. Smith, "Method and results for optimizing the MOPITT methane bandpass," *Appl. Opt.*, Vol. 36, pp. 4285-4291, (June 1997).

12. M.W. Smith, S. R. Shertz, N. Delen, "Remote sensing of atmospheric carbon monoxide with the MOPITT Airborne Test Radiometer (MATR)," *Proc. SPIE* ,Vol. 3756, pp. 475-485, (July, 1999).

13. W. L. Wolfe and G. J. Zissis, eds., *The Infrared Handbook*, Table 3-17, pp. 3-36, Ann Arbor, MI: Infrared Information Analysis Center (3rd printing 1989), ISBN 0-9603590-1-X.

DISTRIBUTION

1	MS0406	Jeffrey A. Mercier	5717
1	MS0406	Mark W. Smith	5717
1	MS0971	Robert D. M. Tachau	5737(electronic copy)
1	MS0980	Toby O. Townsend	5710 (electronic copy)
1	MS0899	Technical Library	9536 (electronic copy)
1	MS0359	D. Chavez, LDRD Office	1911 (electronic copy)